

Scale-invariant dynamics in a purely deterministic Game of Life model

Hakan Akgün,¹ Xianquan Yan (颜显权),^{2,3} Tamer Taşkiran,⁴
Muhamet İbrahimî,⁵ Ching Hua Lee,^{2,*} and Seymur Jahangirov^{4,†}

¹*Department of Physics, Bilkent University, Ankara, Turkey*

²*Department of Physics, National University of Singapore, Singapore 117551*

³*Department of Computer Science, National University of Singapore, Singapore 117417*

⁴*UNAM, Institute of Materials Science and Nanotechnology, Bilkent University, Ankara 06800, Turkey*

⁵*Laboratory of Artificial and Natural Evolution (LANE), Department of Genetics and Evolution, University of Geneva, 1211 Geneva, Switzerland*

(Dated: June 10, 2025)

Scale invariance is a key feature that characterizes criticality in complex dynamical systems, which often organize into structures exhibiting no typical size and/or lifespan. While random external inputs or tunable stochastic interactions are typically required for showcasing such criticality, the question of whether scale-invariant dynamics can emerge from purely deterministic interactions remains unclear. In this work, we discover highly affirmative signatures of critical dynamics in equal-state clusters that emerge in the *logistic* Game of life (GOL): an extension of Conway's GOL into a Cantor set state space that is nevertheless deterministic. We uncover at least three types of asymptotic behavior, i.e. phases, that are separated by two fundamentally distinct critical points. The first critical point – associated with a peculiar form of self-organized criticality – defines the non-analytic boundary between a sparse-static and a sparse-dynamic asymptotic phase. Meanwhile, the second point marks an enigmatic deterministic percolation transition between the sparse-dynamic and a third, dense-dynamic phase. Moreover, we identify distinct power-law distributions of cluster sizes with unconventional critical exponents that challenge the current paradigms for critical behavior. Overall, our work concretely paves the way for studying emergent scale invariance in purely deterministic systems.

I. INTRODUCTION

Scale invariance is a hallmark of critical behavior in dynamical systems [1–8]. In particular, spatially extended systems driven by local interactions exhibit scale-invariant dynamics by organizing in clusters with no characteristic size and/or duration. Typically, such behavior emerges either from the intrinsic characteristics of interactions – i.e. known as self-organized criticality – or, from an external tuning parameter that modulates the strength of interactions, – i.e. parameter-driven criticality [9]. The former has been identified in sandpile [10, 11], forest-fire [12] and earthquake [13] cellular automaton models, whereas the latter has been observed in models exhibiting percolation transitions [14–21] and has been characterized by universal scaling laws. However, given that such models typically include random external inputs, noise, or stochastic components in their dynamics, the question of whether scale-invariant dynamics can emerge from purely deterministic interactions remains unclear.

To address this question, studies have examined the emergence of criticality in deterministic systems from various perspectives. For example, deterministic interactions governing invasion [22] and bootstrap percolation [16, 23], random walks [24–29], fractal networks [30–32] have been investigated. Moreover, a deterministic

ansatz for fractal-like critical snapshots [33] has been proposed. It has been also shown that kinetic constraints to deterministic models may bring directed percolations [34, 35]. Lastly, other studies have drawn parallels between transitions in deterministic coupled map lattices [36–38] and percolation phenomena. Despite these works, clear evidence of purely deterministic scale-invariant cluster dynamics remains elusive, and this behavior has not been systematically investigated.

On the other hand, Conway's Game of Life (GOL) is a simple deterministic cellular automaton that has served as a playground for studying critical dynamic behavior. This discrete dynamical system – defined by local parallel interactions (i.e. rules) among binary states in a square lattice of sites [39] – has often been a starting point for studying phenomena related to artificial life [40, 41], ecology [42], and self-organization [43–46]. Importantly, the underlying interactions of this system have also been ‘probed’ for their capacity to exhibit self-organized criticality [47, 48], or to undergo critical phase transitions [49–53]. Regarding the latter, prior studies have extended GOL dynamics with control parameters that, by incrementally modifying the rules away from the original system [49–51, 54, 55], suggest that Conway's GOL rules are strongly associated with scale-invariant dynamics. However, while such variations employ stochastic components, this system has never been investigated in the context of deterministic critical behavior.

In this paper, we analyze the scale-invariant dynamics that emerge due to the phase transitions occurring in the

* phylch@nus.edu.sg

† seymur@unam.bilkent.edu.tr

logistic GOL [45]: a deterministic extension inspired by the logistic map [56], where a control parameter changes the rate of update of sites by expanding the initially binary state space into a Cantor set. As the parameter ‘drifts’ the system away from Conway’s GOL, the asymptotic dynamics of this system changes from a sparse-static (I) phase (like Conway’s GOL) to a sparse-dynamic (II), and then a dense-dynamic (III) phase. We identify the points that separate these three distinct dynamical regimes numerically and study their critical properties by in-depth analyses of cluster dynamics. We find that the critical point separating phases I and II defines the non-analytic boundary of a peculiar form of self-organized criticality in the sparse-dynamic phase, where quiescent clusters surrounded by active sites follow a power-law distribution (Fisher exponent $\tau \simeq 2.9$). Moreover, detailed cluster analyses at the critical point separating phases II and III ($\tau \simeq 1.81$), indicate a continuous, deterministic percolation transition.

Overall, we pinpoint a purely deterministic system – i.e. system devoid of noise, random external inputs, or stochasticity in interactions – which displays scale-invariant dynamics in both of its typical forms. Beyond showcasing critical behavior, the logistic GOL introduces a broad range of tunability. This tunability allows for precise control of the cluster shapes and the ‘tail-fatness’ of cluster size distributions, studied here for the first time in a spatially extended deterministic system. Moreover, the unconventional Fisher exponent of our percolation transition ($\tau < 2$) violates the hyperscaling constraints [17, 18], and hence challenges standard assumptions of critical phenomena.

The paper is organized as follows. In Sec. II A we discuss how we extend Conway’s GOL to the logistic GOL. In Sec. II B, we report results from simulations of the logistic GOL and identify the different asymptotic dynamical regimes separated by critical points. In Sec. II C and Sec. II D, we characterize the critical points through extensive cluster analyses and power law distributions. Lastly, in Sec. III we provide a summary of the deterministic critical behavior identified here.

II. RESULTS

A. The Logistic Game of Life

The original Conway’s GOL is defined on a square lattice of sites, where each site goes through the parallel updating scheme:

$$s_j^{t+1} = s_j^t + \Delta s_j, \quad (1)$$

where $s_j^t \in \{0, 1\}$ corresponds to the state of j^{th} site at time point t . Δs_j denotes the quantity to be added to update the state from s_j^t to s_j^{t+1} , and is a function of s_j^t itself and the sum of states in its Moore neighborhood m_j^t (Fig. 1a left panel), with $0 \leq m_j^t \leq 8$. According to

the finite-difference notation of Eq. (1), a site in Conway’s GOL can experience three possible updates: decay ($\Delta s_j = -s_j$ when $m_j < 2$ or $m_j > 3$), stability ($\Delta s_j = 0$ when $m_j = 2$), or growth ($\Delta s_j = 1 - s_j$ when $m_j = 3$) (Fig. 1a middle).

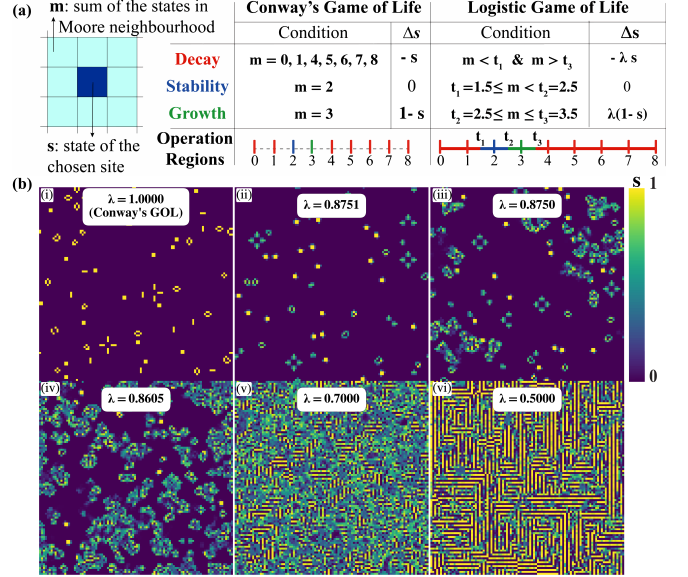


Figure 1. **The logistic Game of Life.** (a) Short summary of the rules of Conway’s GOL (middle) and the logistic GOL (right). In the latter, a parameter λ tunes the rate of update of sites. (b) Illustrative snapshots of the asymptotic states in both Conway’s Game of Life ($\lambda = 1$) and the Logistic Game of Life across various λ values. Each configuration was initialized with a random array on a 1024×1024 grid and evolved for 10,000 time steps with periodic boundary conditions.

On the other hand, the logistic GOL [45] stands as a prominent candidate for investigating deterministic scale invariant dynamics in 2D systems. This system introduces a control parameter, λ , which tunes the update dynamics by rescaling the growth/decay rate of each site as $\Delta s_j^t \rightarrow \lambda \Delta s_j^t$, where $0 < \lambda \leq 1$. The case $\lambda = 1$ corresponds to the original limit of Conway’s Game of Life (Fig. 1a, right).

An important consequence of λ in the logistic GOL is that the previously binary state space of the automaton expands into a Cantor set. To see this, one may define a simple representation that associates the three possible updates to discrete operators, respectively to decay (D), stability (S) and growth (G), such that:

$$\mathbf{Ds} := (1 - \lambda)s, \quad \mathbf{Ss} := s, \quad \mathbf{Gs} := (1 - \lambda)s + \lambda. \quad (2)$$

These discrete operators show how the state s of a site may be updated, based on λ and the nearest neighborhood (Fig. 1a right). If we apply these operators to an initial set of $\{0, 1\}$ once, they give rise to a larger set $\{0, 1 - \lambda, \lambda, 1\}$. Again, applying operators to the new set gives rise to $\{0, (1 - \lambda)^2, (1 - \lambda) - (1 - \lambda)^2, 1 - \lambda, \lambda, \lambda + (1 - \lambda)^2, \lambda, 1 - (1 - \lambda)^2, 1\}$. Repeating this recursively would

lead to a λ dependent Cantor set in the range $[0, 1]$ (see Fig. 8a in Appendix IV B). For later use, we define the *order* of each element in the Cantor set as the number of times a **D** or **G** operator has been applied to obtain it, starting from 0 or 1. For example, **GG** 0 = $1 - (1 - \lambda)^2$ is a second-order Cantor value (Fig. 8a).

A second consequence of λ is that, due to the expanded state space, the space of neighborhood sums m (which determine how sites are updated) is also expanded. In the logistic GOL, possible m values span the range $[0, 8]$ and comprise an eight-fold convolution of the Cantor set. To account for this, we assign two unit-length intervals centered at $m = 2$ and $m = 3$ as the neighborhood sum regions of stability and growth, respectively (Fig. 1b). We denote the limits of these intervals by $t_1 = 1.5$, $t_2 = 2.5$, and $t_3 = 3.5$, such that sites get updated in the following fashion:

$$s_j^{t+1} = \begin{cases} \mathbf{S}s_j^t = s_j^t & \text{if } t_1 \leq m_j^t < t_2 \\ \mathbf{G}s_j^t = (1 - \lambda)s_j^t + \lambda & \text{if } t_2 \leq m_j^t \leq t_3 \\ \mathbf{D}s_j^t = (1 - \lambda)s_j^t & \text{otherwise} \end{cases} \quad (3)$$

The rules of Conway's and logistic GOL are summarized in Fig. 1a, and snapshots of the asymptotic behavior of the logistic GOL at various λ are displayed in Fig. 1b. As previously identified [45], the dynamic and asymptotic behavior of logistic GOL for $0.875 < \lambda < 1$ is similar to Conway's GOL, where the system settles to a sparse inactive asymptotic state. Whereas, for $\lambda \leq 0.875$, the system possesses active asymptotic states, which increasingly cover the system as λ decreases (Fig. 1b). While previous work has discussed the asymptotic density around $\lambda = 0.875$ and the maze-like striped patterns at $\lambda < 0.7$ [45], no proper critical behavior has been identified. Here, we identify two points with distinct critical properties – marking the boundaries between different asymptotic phases (Fig. 1b(iii) and (iv)) – and characterize them through cluster analyses and power-law distributions.

To study the critical properties of the asymptotic dynamics, we perform simulations of the logistic GOL where the state space is truncated up to the 10th order of the Cantor set. In other words, during simulations, any state with a higher-order Cantor value is ‘lumped’ into the nearest Cantor value of order ≤ 10 (see Appendix IV B for implementation).

B. Signatures of Critical Behavior

In this section, we study the asymptotic behavior of the logistic GOL, which exhibits remarkable changes as the control parameter λ ‘drifts’ the system away from Conway's GOL (see the different panels in Fig. 1b). To investigate whether such changes in the asymptotic behavior are related to critical phenomena, we define three quantities that characterize the system.

First, we define an *activity* (A^t) order parameter of the following form:

$$A^t := 1 - \frac{1}{N^2} \sum_j \delta_{s_j^t, s_j^{t-\bar{t}}} \quad (4)$$

where N denotes the length of the square lattice, $\delta_{i,j}$ denotes the Kronecker delta, and the sum is over all sites. A^t is thus defined to denote the fraction of cells that change states after a time lag interval \bar{t} , serving as a measure of lattice's autocorrelation. In the following, we set $\bar{t} = 60$ to exclude asymptotic-state oscillators with periods that are divisors of 60 [57]. We then average the activity over time and ensemble to obtain $\langle A \rangle$. Thus, $\langle A \rangle = 1$ indicates that there is no autocorrelation between the states and their time-lagged counterparts (as expected from a fully active state), whereas $\langle A \rangle = 0$ reflects perfect autocorrelation, i.e. the grid's time-lagged version is identical to the current state.

Second, we use the definition of Eq. (4) to characterize the spatio-temporal variation of activity through the *susceptibility*, defined as the fluctuation of the order parameter:

$$\langle \chi \rangle := \langle A^2 \rangle - \langle A \rangle^2. \quad (5)$$

Analogous to magnetic systems, the susceptibility measures how uniformly the activity is distributed across the lattice. A system comprising of only a few localized active sites is characterized by a high susceptibility, whereas a uniform distribution of active sites leads to a vanishing susceptibility.

Third, we define *clusters* to identify groups of equal-state sites that are connected through their direct nearest neighbors, i.e. up, down, left or right first neighbors. More precisely, a cluster C^t denotes a set of sites in the lattice such that, for any two sites $j, j' \in C^t$, there exists at least one sequence $\{j, k, l, \dots, j'\}$ where

$$s_j^t = s_k^t = s_l^t = \dots = s_{j'}^t, \quad (6)$$

and each site is direct nearest neighbor with at least one other site in C^t . Moreover, C^t is defined such that it is the maximal set of connected sites satisfying the clustering condition, and no subset $\bar{C}^t \subsetneq C^t$ is considered a separate cluster. Additionally, we define the size of a cluster S^t , denoting the number of sites in the cluster, i.e. the *cardinality* of C^t :

$$S^t = n(C^t). \quad (7)$$

Finally, the cluster size ranking at a given time step t is defined by the ordering $S_1^t \geq S_2^t \geq S_3^t \geq \dots \geq S_i^t \geq \dots$, where the index i here indicates the size rank of the cluster. The cluster sizes are then averaged over time and ensemble to obtain $\langle S_i \rangle$.

In Fig. 2, we report the numerically computed asymptotic quantities of $\langle A \rangle$, $\langle \chi \rangle$ and $\langle S_1 \rangle$ for the logistic GOL, where λ is a control parameter. We focus on the parameter region $0.8 < \lambda < 0.9$, where we notice signs of critical

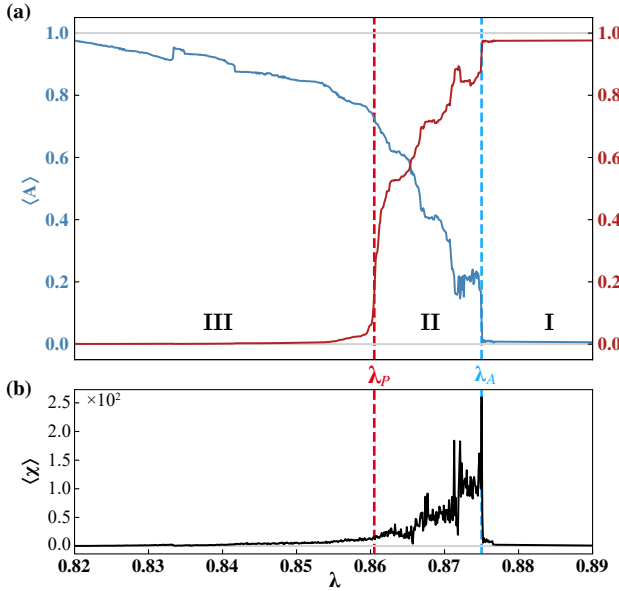


Figure 2. Three distinct asymptotic phases in the logistic GOL separated by two critical points. (a) Asymptotic averaged activity $\langle A \rangle$ (solid blue) and the size of the largest cluster $\langle S_1 \rangle / N^2$ (solid red) computed against λ . The data indicates two critical points: (i) $\lambda_A = 0.8750$ (blue dashed line), the boundary between a sparse-static (I) and sparse-dynamic (II) asymptotic phase; (ii) $\lambda_P = 0.86055$ (red dashed line), where fragmentation of the largest cluster defines the boundary between phase II a dense-dynamic (III) phase. (b) The susceptibility of activity $\langle \chi \rangle$, plotted against λ , hits its maximum at λ_A .

behavior at $\lambda_P = 0.86055$ and $\lambda_A = 0.8750$, and identify three distinct asymptotic phases of the system. In the following, we describe the changes of the system as λ decreases.

1. λ_A : Phase transition in asymptotic activity

First, we discuss how the average asymptotic activity $\langle A \rangle$ changes in the logistic GOL as λ is tuned down (blue data points in Fig. 2a). We observe that $\langle A \rangle \simeq 0$ for $\lambda > \lambda_A = 0.8750$, indicating that, in this parameter range, the logistic GOL comprises inactive asymptotic states. Indeed, similarly to Conway's GOL, the system settles to a sparse-static phase, i.e. a phase that is mostly populated by the *vacuum* background of quiescent states, and sparsely populated by stable blocks and periodic oscillators (panels (i) and (ii) in Fig. 1b). At $\lambda = \lambda_A$ we observe a sudden increase in activity, which indicates that the asymptotic dynamics becomes fundamentally different. In the $\lambda \leq \lambda_A$ range, the system does not settle into a static phase (panel (iii) in Fig. 1b), but rather it persists indefinitely in the thermodynamic limit. Incidentally, this reflects the recovery of the ergodic hypothesis, where the system no longer converges to a single final configuration but visits all the possible configurations.

Moreover, we find that the susceptibility $\langle \chi \rangle$ (Fig. 2b) reaches its maximum at $\lambda = \lambda_A$ (blue dashed line in Fig. 2). The sudden jump in $\langle A \rangle$ and maximal $\langle \chi \rangle$ suggest that λ_A is the critical point which marks the static-dynamic transition in the asymptotic behavior of the system. Given that the activity is identically zero on an open interval when $(\lambda > \lambda_A)$, and non-zero when $(\lambda < \lambda_A)$ [45], the identity theorem for real-analytic functions implies that λ_A must be a non-analytic (singular) point of this phase transition – similar to the behavior observed in the two-dimensional Ising model. This non-analyticity is formally discussed in Appendix IV C.

Besides defining the transition point between static and dynamic phases in the logistic GOL, the asymptotic susceptibility $\langle \chi \rangle$ provides additional insights on the nature of this transition. The fact that $\langle \chi \rangle$ increases sharply from zero to a maximum as λ hits λ_A (Fig. 2b), indicates that the asymptotic activity at the transition point is initially localized in a very low number sites, and that the lattice is otherwise similar to the static phase in $\lambda_A < \lambda \leq 1$ (panel (iii) in Fig. 1b). Moreover, the drop of $\langle \chi \rangle$ as λ decreases below λ_A , indicates that the activity becomes increasingly more spread in space, until the lattice becomes homogeneously active and $\langle \chi \rangle$ hence vanishes (panels (iv) and (v) in Fig. 1b and Fig. 2b).

2. λ_P : Phase transition in asymptotic cluster size

Next, we identify a third asymptotic phase that emerges as λ is tuned down even further. In particular, we investigate the how the size of the largest cluster $\langle S_1 \rangle / N^2$ – i.e. corresponding to the vacuum cluster of quiescent states in the lattice – changes against λ . The vacuum cluster (red in Figure 2a) covers most of the grid when $\lambda > \lambda_A$. As λ is tuned down below λ_A , the size of the largest vacuum cluster drops, approximately following the inverse pattern of $\langle A \rangle$. However, as λ decreases further, the behavior of $\langle S_1 \rangle / N^2$ becomes remarkably different as compared to $\langle A \rangle$. The largest cluster of quiescent states experiences a sharp decrease, where the strongest drop occurs at $\lambda_P \approx 0.86055$, defining another critical point.

This sharp decrease in the size of the largest cluster (red dashed line in Fig. 2) is important because it indicates a transition from an asymptotic dynamical phase with the vacuum cluster spanning the lattice, to a dynamical phase where there is no spanning cluster, and is reminiscent of a percolation transition. We study this transition in detail below in Sec. II C. We additionally note that, the decrease in $\langle \chi \rangle$ (Fig. 2b) as λ goes below λ_P implies a more uniform activity within the lattice, and is another indicator of this third asymptotic phase.

λ	Transition	Neighborhood
0.86055	$G \leftrightarrow D$	$t_3 \approx -3\lambda^5 + 16\lambda^4 - 34\lambda^3 + 33\lambda^2 - 17\lambda + 8$
0.86055	$S \leftrightarrow D$	$t_1 \approx -3\lambda^5 + 16\lambda^4 - 34\lambda^3 + 33\lambda^2 - 17\lambda + 6$
0.8750	$G \leftrightarrow D$	$t_3 = 4\lambda$
0.8750	$S \leftrightarrow D$	$t_1 = 4[1-\lambda] + 1$

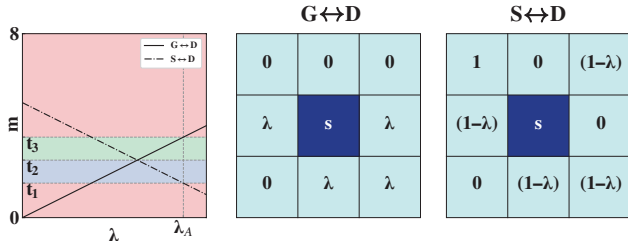


Figure 3. Operational transition neighborhoods at critical points. The table above summarizes the neighborhood sums of the critical points at the operational thresholds ($t_1 = 1.5$, $t_2 = 2.5$, $t_3 = 3.5$). The panel below shows neighborhoods undergoing transition, with unordered individual site values (as only the sum m determines the operational region) highlighted around $\lambda_A = 0.875$, while the lower left panel illustrates the numerical evolution of these neighborhoods as λ varies between $0 < \lambda < 1$. At the critical points, the polynomial neighborhoods switch regimes— $G \leftrightarrow D$ and $S \leftrightarrow D$ —corresponding to transitions in neighborhood sums $t_3 \leftrightarrow t_1$ and $t_2 \leftrightarrow t_1$, respectively, highlighting their role in the phase transition at λ_A . For a similarly detailed view of the neighborhood at λ_P , see Appendix IV D

3. Determination of phase transition points from GOL operation regions

The increase in activity and the decrease of the vacuum cluster’s size indicates that the average density of the system increases as λ is tuned down (see also Fig. 1b). This occurs because, as λ decreases, there are several neighborhood configurations which change their operation regions (Fig. 3). For example, a neighborhood m_j consisting of $4 \times \lambda$ sites and 4×0 sites would ‘act’ to decay the central site if $\lambda > \lambda_A$ because $m_j = 4\lambda > t_3 = 3.5$. However, for $\lambda \leq \lambda_A$, then $m_j \leq t_3$, indicating that the central site will experience growth instead of decay. In a similar fashion, as λ decreases, another neighborhood with $m_k = 1 + 4(1-\lambda)$ changes the operation region from decay to stability at λ_A . In this case, the central site will decay when $\lambda > \lambda_A$, as $m_k < t_1 = 1.5$; and it will remain stable when $\lambda \leq \lambda_A$, as $m_k \geq t_1$. Note that there is a large set of neighborhood sums which changes operation regions as λ is tuned down further, and it is these changes which alter the dynamics of the logistic GOL [45]. The main neighborhood sums that change operation regions at $\lambda = \lambda_P$ are reported in Fig. 3.

While the non-analytic transition at λ_A reflects the influence of a fixed first-order Cantor-set polynomial Moore

neighborhood, the fragmentation of the vacuum cluster near λ_P emerges due to gradual neighborhood changes from higher-order polynomials. These gradual neighborhood transitions with changing λ govern the evolution of cluster shape, size, and scaling. A more detailed discussion is provided in Appendix IV D.

C. A deterministic percolation transition in the logistic GOL

Motivated by the interesting asymptotic behavior of the size of the largest cluster in the logistic GOL, we here complement these findings by studying the cluster dynamics of the system as λ approaches $\lambda_P = 0.86055$ *from below*. By investigating the sizes and geometrical properties of clusters, we find that λ_P is the critical point of a percolation transition that separates two distinct phases of asymptotic behavior: a dynamic phase with no spanning cluster ($\lambda \leq \lambda_P$) and a dynamic phase with a giant vacuum cluster that spans the lattice ($\lambda_P < \lambda < \lambda_A$).

We examine the size and geometrical properties of the largest clusters in the parameter range $\lambda \in [0.850, 0.875]$, where for convenience, we focus on the five largest clusters (Fig. 4). First, we note that the highest-ranked clusters, i.e. clusters with $\{\langle S_1 \rangle, \dots, \langle S_5 \rangle\}$, are all composed of zero states (see top and bottom panels in Fig. 4a). When $\lambda \simeq 0.85$, all clusters exhibit comparable sizes but remain small relative to the lattice size (Fig. 4b). As λ increases and approaches λ_P , the size of each cluster increases, and the size of the second largest cluster hits maximum at $\lambda = \lambda_P$ (purple curve in Fig. 4b). When $\lambda > \lambda_P$, the size of the largest cluster increases as they merge (red regions in Fig. 4a and inset in Fig. 4b), while sizes of lower ranked clusters drop significantly.

1. Critical evolution of cluster capacity dimension

Next, we analyze how the shapes of the largest clusters evolve with λ through their capacity dimensions. This ‘probes’ whether clusters become scale-invariant near λ_P . Employing the box-counting method, the capacity dimension d_c of the clusters is given by:

$$d_c = - \lim_{\epsilon \rightarrow 0^+} \frac{\log \mathcal{N}(\epsilon)}{\log \epsilon} \quad (8)$$

where $\mathcal{N}(\epsilon)$ denotes the minimum number of boxes of size ϵ needed to cover the cluster (see Appendix IV E 1 for methods). A capacity dimension of $d_c \sim 1$ indicates that cluster shapes are more chain-like and sparse, while $d_c \sim 2$ indicates that clusters are more area-like and dense. The capacity dimensions of the largest five clusters are plotted against λ in Fig. 4c. The obtained d_c converge towards each other as λ approaches λ_P from below, signifying scale invariance at criticality. But once $\lambda > \lambda_P$, the capacity dimensions diverge strongly: the

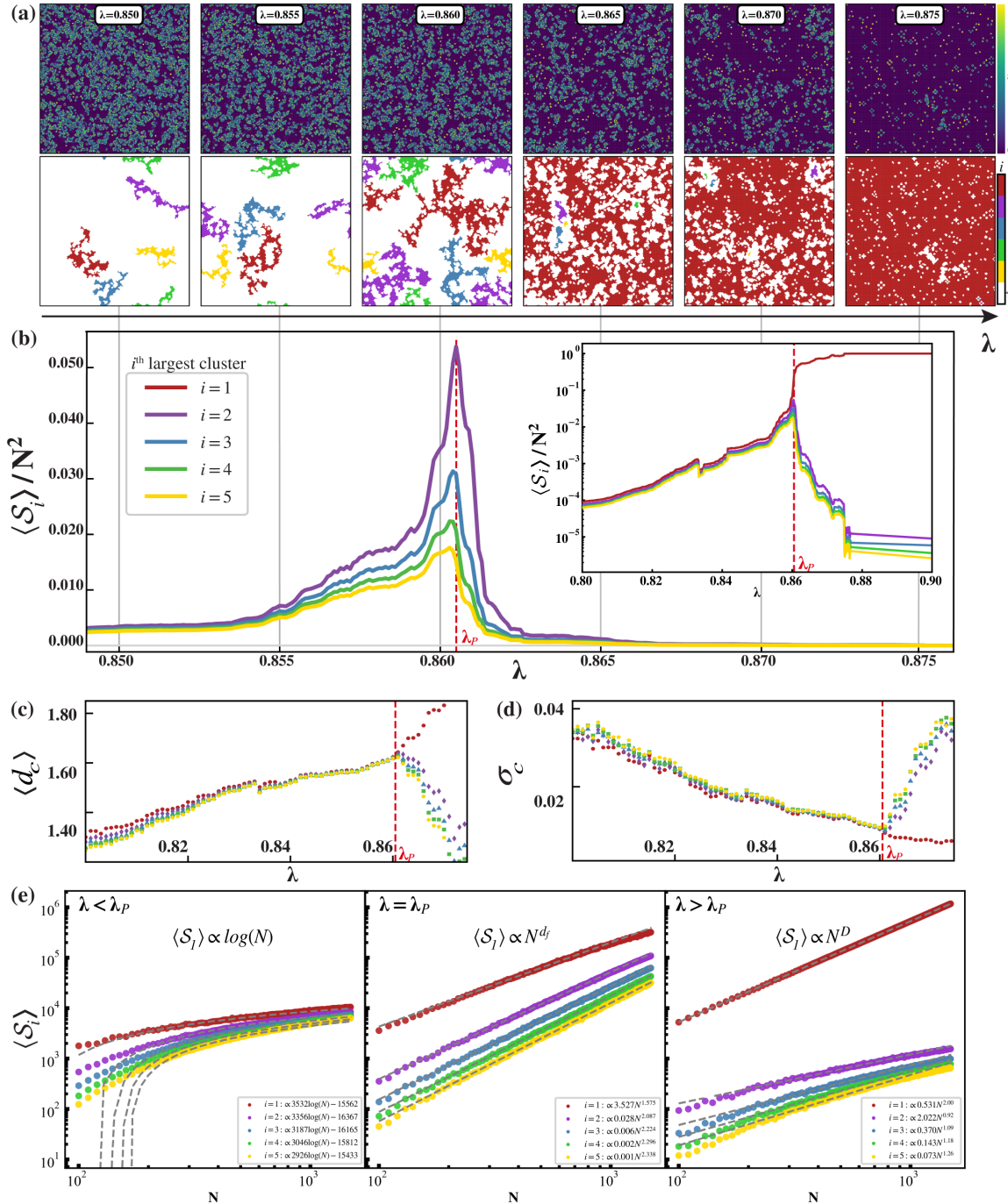


Figure 4. Deterministic cluster dynamics reveals a percolation transition in the logistic GOL. (a) Top panels display snapshots of the asymptotic states of the logistic GOL at distinct λ values in the range [0.850, 0.875]. Bottom panels show the corresponding five largest clusters masked in different colors (ranking in panel b). (b) Sizes of the largest clusters $\langle S_2 \rangle \sim \langle S_5 \rangle$ plotted against λ , where the index i indicates the size rank of the cluster. The curves differ only by scaling when $\lambda < \lambda_P$. The inset displays the logarithmic evolution of cluster sizes, with the largest zero-state cluster (dark red) percolating as λ increases. The evolution of (c) capacity dimensions d_c of the largest clusters and their (d) corresponding standard deviations σ_c computed as functions of λ . (e) Scaling behavior of the largest cluster with lattice size (N) around λ_P . In the ‘subcritical’ regime ($\lambda < \lambda_P$, left), cluster sizes $\langle S_i(N) \rangle$ follow a logarithmic trend. Around the critical point ($\lambda = \lambda_P$, middle), the clusters scale as power laws, where the exponent of the largest cluster defines the fractal dimension d_f . In the ‘supercritical’ regime ($\lambda > \lambda_P$, right), the largest cluster $\langle S_1 \rangle$ scales with the system’s dimension, spanning the lattice. The associated fits are shown with gray dashed lines.

largest cluster's capacity dimension increases, while the other clusters' capacity dimensions decrease.

Moreover, we examine how different samplings of the same clusters change at each λ by calculating the standard deviation σ_c of the capacity dimension. This allows us to quantify the stability of the shapes within a given cluster distribution. As shown in Fig. 4d the σ_c of every cluster decreases and reaches its minimum as λ approaches λ_P from below. When $\lambda > \lambda_P$, the largest cluster's standard deviation remains stable over different samplings while σ_c of the other clusters increase. Such fluctuations are also reflected in the susceptibility profile seen in Fig. 2b.

From the above analysis, it is evident that the highest-ranked clusters undergo a percolation transition at λ_P . Indeed, as λ approaches λ_P from below, the capacity dimensions of all clusters increase: they attain the same value ($d_c \approx 1.610$) and a minimal standard deviation ($\sigma_c \approx 0.01$). In other words, when $\lambda = \lambda_P$, the shape of a cluster at a given time point is similar to the shape of any other cluster at any time point. Therefore, the clusters tend towards the same shape with respect to each other and only differ in size, providing strong evidence for scale invariance at λ_P . Then, when $\lambda > \lambda_P$, the shapes of the clusters change drastically with respect to each other (Fig. 4c) and with respect to their different samples (Fig. 4d). Here, the increase of the largest cluster's size and capacity dimension (dark red in Fig. 4a,c and Appendix Fig. 11) signals the percolation transition, while the sizes and capacity dimensions of the smaller clusters decrease as they become smaller and more chain-like.

2. Critical scaling of cluster sizes

To further support the hypothesis that the transition at λ_P is percolation-like, we investigate how the largest cluster's size $\langle S_1 \rangle$ scales with the lattice size N as we approach λ_P (Fig. 4e), where we find that the scaling is the same as in classical percolation models [17, 18]. While relegating the methods to Appendix IV E 2, here we report the observed scaling relationships:

$$\langle S_1(N) \rangle \sim \begin{cases} \log N, & \text{for } \lambda < \lambda_P, \\ N^{d_f}, & \text{for } \lambda = \lambda_P, \\ N^D, & \text{for } \lambda > \lambda_P, \end{cases} \quad (9)$$

where $D = 2$ denotes the dimension of the system, and $d_f < D$ defines what is referred as the fractal dimension. In the 'subcritical' regime ($\lambda < \lambda_P$), the largest cluster grows logarithmically with system size (left panel in Fig. 4e), meaning that there can be no giant cluster spanning the lattice. At the critical point ($\lambda = \lambda_P$), the largest cluster follows a fractal scaling, reflecting the self-similar nature of the percolating cluster (Fig. 4e middle panel). The fitted fractal dimension is $d_f \approx 1.575$ with a standard deviation of $\sigma_f \approx 0.1$, attributed to deviations

from the exact critical point λ_P beyond five decimal precision, which also cause deviations in the large N regime. In the 'supercritical' regime ($\lambda > \lambda_P$), the largest cluster grows with the system dimension ($D = 2$), indicating the formation of a percolating cluster that spans the lattice (Fig. 4e right panel).

Besides the scaling relations governing $S_1(N)$, the scalings of lower-ranked clusters $\langle S_i(N) \rangle$ indicate that, as $N \rightarrow \infty$, $\langle S_i(N) \rangle$ diverge to infinity only at the critical point $\lambda = \lambda_P$ (Fig. 4e). Note that the divergence of the second-largest peak is explicitly illustrated in Fig. 12 (see Appendix IV E 3 for details). Taken together, all the analyses of largest clusters (Fig. 4) indicate the emergence of percolating cluster and a phase transition [58] at $\lambda = \lambda_P$.

D. Cluster size distributions near the critical points

Having previously established the scaling properties of the largest clusters with system size, we next investigate the extent to which cluster size *distributions* near the critical points λ_P and λ_A follow power laws. To do this, we perform numerical simulations of the logistic GOL to compute the distribution of cluster sizes, $p(S)$, in the vicinity of each critical point (Fig. 13, Appendix).

As a brief overview, at $\lambda_P = 0.86055$, $p(S)$ seems to follow a power law, while for other nearby λ values, distributions appear as stretched exponentials (Fig. 13a). On the other hand, there are multiple λ values close to $\lambda_A = 0.8750$ where the distributions are reminiscent of power laws, but only if the largest vacuum clusters are disregarded (Fig. 13b). While relegating technical aspects on computations of $p(S)$ to Appendix IV E 4, below we leverage quantitative methods to test whether such distributions are indeed best described by power laws.

The scaling of power-law data is rarely valid across the entire domain of cluster sizes. More often, the power law applies only for values greater than some lower bound S_{\min} , i.e., only the 'tail' follows a power law. In such cases, the cluster size distribution is expected to follow:

$$p(S) = \frac{S^{-\tau}}{\zeta(\tau, S_{\min})} \quad \text{for } S \geq S_{\min} \quad (10)$$

where τ is the power-law exponent (the Fisher exponent [59]), S_{\min} is the lower cutoff, and $\zeta(\tau, S_{\min})$ denotes the generalized zeta function

$$\zeta(\tau, S_{\min}) = \sum_{S=S_{\min}}^{\infty} S^{-\tau} = \sum_{S=0}^{\infty} (S + S_{\min})^{-\tau}. \quad (11)$$

The corresponding *complementary cumulative distribution function* (cCDF) then reads:

$$\mathcal{F}(S) = \sum_{S'=S}^{\infty} p(S') = \frac{\zeta(\tau, S)}{\zeta(\tau, S_{\min})}. \quad (12)$$

Using the numerically computed cCDF (Appendix IV E 4), we determine the Fisher exponent τ and the lower bound S_{\min} by employing the Kolmogorov-Smirnov (KS) method [60–62]. In addition to finding the optimal values of τ and S_{\min} , the KS method assesses how well the power-law model fits to the data in comparison to other fat-tailed distributions. Details on the implementation of the KS method are provided in Appendix IV F.

Initially, we apply the KS method to the cluster size distributions for λ values in the vicinity of λ_P . In this range, the logistic GOL unlocks dynamic control over cluster behavior, enabling precise tuning of the tail fatness in the cluster distribution through the tuning parameter λ . As shown in Fig. 5a, the tail of the cCDFs undershoots the power-law line when $\lambda < \lambda_P$. As λ increases, the number of zero clusters and the variance of cluster sizes increase, resulting in a fatter tail (Fig. 5b). However, at $\lambda = \lambda_P$, we observe that the tail fits with a power law with exponential cutoff (Fig. 5b). This cutoff is due to finite-size effects (Fig. 15). Further increases in λ lead to the loss of perfect linearity of the cluster size distribution (Fig. 5c), supporting the assertion that λ_P is the critical point for the emergence of a giant cluster. Beyond this point, the largest vacuum cluster separates from the rest of the distribution and begins to percolate. As S_1 grows to be comparable to the system size N^2 , it diverges from the main body of the distribution (arrow in Fig. 5d). This evolution is also evident through simulation snapshots in Fig. 4a.

The fit results of the KS method for cluster distribution at $\lambda = \lambda_P$ yield a power-law distribution with exponential cutoff, with the following coefficients:

$$\lambda_P = 0.86055 : \begin{cases} \tau = 1.81 \pm 0.03 \\ S_{\min} = 560 \pm 150 \end{cases} \quad (13)$$

The plausibility of the optimal power-law fit to the numerical data is confirmed by the KS method. Additionally, log-likelihood ratio tests whether alternative fat-tailed distributions (*e.g.*, exponential, stretched exponential, or log-normal) offer a better fit than the power law. As shown in Table II, Appendix IV F 4, the power-law distribution with an exponential cutoff best characterizes the system at λ_P .

Next, we discuss the cluster size distributions in the vicinity of λ_A . As previously mentioned, in this range the lattice is dominated by the largest percolating cluster. However, we find that the distribution of other smaller clusters exhibits interesting behavior. Therefore, when applying the KS method to the cluster size distributions near λ_A , we always neglect the largest cluster by ‘trimming out’ the separated part of the distribution (arrow in Fig. 5).

As λ approaches λ_A from below, the trimmed cluster size distribution displays similar behavior as in the vicinity of λ_P (Fig. 6). As shown in Fig. 6a,b, the tail approaches the power-law line from below. At $\lambda = \lambda_A$,

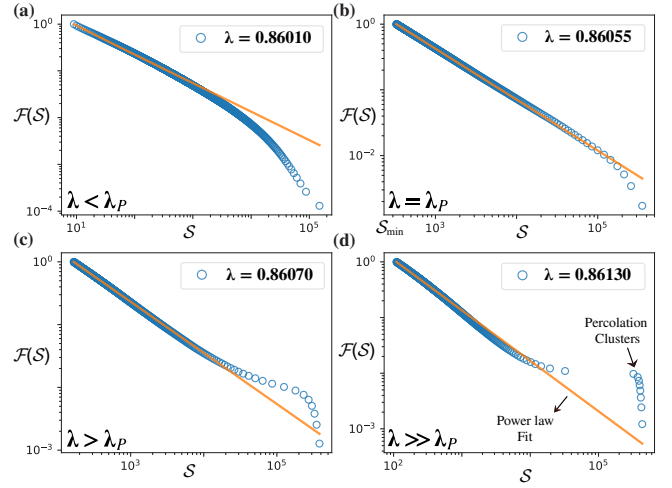


Figure 5. Behavior of cluster size distribution around $\lambda_P = 0.86055$. The empirical complementary cumulative distribution function (cCDF) with *logarithmic-binning* [60] is shown in blue, with the fitted power-law in orange, for λ values (a) below, (b) close and (c)(d) above λ_P . The x-axis starts from the optimal S_{\min} determined by the KS method (see text). The cluster size distribution becomes a power law (with exponential cutoff) only very close to the critical point λ_P .

the cluster size distribution follows a power law (Fig. 6c) which, in contrast to λ_P , does not have an exponential cutoff. Then, as λ increases above λ_A , the system transitions to an inactive phase, resulting in the disappearance of cluster dynamics (Fig. 6d). The corresponding power law parameters fitted by the KS method read:

$$\lambda_A = 0.8750 : \begin{cases} \tau = 2.9 \pm 0.1 \\ S_{\min} = 11 \pm 3 \end{cases} . \quad (14)$$

Similar to the previous case, the comparison test details for λ_A are provided in Appendix Table II.

Further statistical analyses using the KS method over different parameter values in the range $0.8 < \lambda < 0.9$ are discussed in Appendix IV F 3, where we evaluate the quality of the power-law fits for the cluster size distributions near the critical points. The results of these statistical analyses indicate that:

- At $\lambda_P = 0.86055$, the tail of cluster size distribution follows a power law with exponential cutoff.
- At $\lambda_A = 0.8750$, the tail of cluster size distribution follows a pure power law when the giant vacuum cluster is disregarded.

The different natures of criticality at λ_P and λ_A points are also reflected in their Fisher exponents, τ . At $\lambda = \lambda_P$, where $1 < \tau < 2$, all moments diverge, including the mean $\langle S(\lambda_P) \rangle$. This arises because the percolation behavior causes the bulk of the distribution to be highly concentrated in the tail. In the thermodynamic limit,

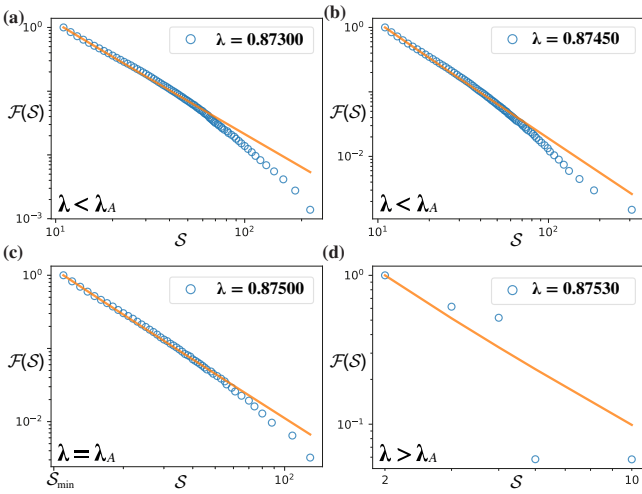


Figure 6. The evolution of cluster size distribution around $\lambda_A = 0.8750$, when the largest vacuum cluster is disregarded. The cCDFs with logarithmic-binning shown in blue, with the fitted power law in orange. The largest vacuum clusters are ignored here and the x-axis starts from the optimal S_{\min} determined by KS method. (a)-(c) The distribution evolves near λ_P by approaching a power law from below and becomes a power law near λ_A . For $\lambda > \lambda_A$ (d), asymptotic activity and cluster formation cease, leading to the disappearance of cluster dynamics.

the tail of the distribution (Fig. 5c) extends to infinity, resulting in $\langle S(\lambda_P) \rangle \rightarrow \infty$. In contrast, at $\lambda = \lambda_A$, where $2 < \tau < 3$, the mean remains finite, and only the variance and higher moments diverge. This means that, unlike λ_P , the critical behavior at λ_A does not constitute of clusters comparable to the system size. Below, we discuss on the potential mechanisms involved in the emergence of such power-law distributions.

1. Contrasting mechanisms for criticality from cluster size distributions

The mechanism behind the percolation transition can be explained as follows. As λ approaches λ_P from below, the system promotes more zero states because several neighborhood sums increase from $m \leq t_3$ to $m > t_3$, inducing decay instead of growth (Section II B). As a consequence, clusters of quiescent states grow continuously with λ until they merge with each other at $\lambda = \lambda_P$. In this respect, the dominance of zero states in the grid and the power law behavior of cluster sizes indicates that λ_P marks the point of a deterministic percolation transition. We moreover note that the cluster size distribution exponent $\tau \simeq 1.81$ found in λ_P is lower than exponents in classical 2D ordinary percolation models ($\tau > 2$), hence the universality class of this transition remains unclear. However, we also note that extremely similar exponents have been observed in interesting scenarios, such as the no-enclave percolation model [19] and the percolation of

sites not visited by a 2D random walk [20].

The mechanism for the emergence of power law around λ_A is fundamentally different from λ_P . Around λ_A , the system is dominated by a vacuum cluster of quiescent states that serves as a ‘playground’ for activity with diverging susceptibility. This susceptible activity spreads in a particular fashion such that it ‘encircles’ quiescent regions in the grid, giving rise to smaller zero-state clusters (Fig. 7). Interestingly, the size of these zero-state clusters encircled by activity follows a power-law distribution, which emerges close to λ_A . Beyond this value, the power-law ceases because the asymptotic activity stops due to more neighborhood sums inducing decay instead of growth.

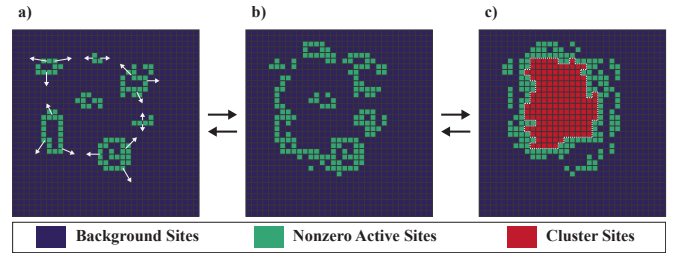


Figure 7. A peculiar form of deterministic, self-organized criticality in the vicinity of λ_A . As λ approaches λ_A from below, the (a) active nonzero cells ‘move’ in a manner that (b) encircles the zero-state background cells and (c) occasionally forms clusters with the associated power law behavior. These steps are two-way: just as clusters are formed, they can also fragment in the same manner.

2. Self-organized criticality in the vicinity of the λ_A

We believe that the power-law behavior in the vicinity of λ_A reflects a form of self-organized criticality (SOC), similar to the one discussed by Bak *et al.* [47][48]. In these studies, it has been shown that the activity clusters follow a power law when the asymptotic state of Conway’s GOL is continually perturbed by altering single sites. In our case, the power-law distribution of zero clusters occurs at multiple points in the region $\lambda \rightarrow \lambda_A^-$ (Fig. 6a,b and Fig. 16 in Appendix IVF3), suggesting scale invariance over a continuous parameter range, similar to the SOC behavior. We speculate that, around λ_A , the logistic GOL administers ‘perturbations’ to itself continually via neighborhood configurations of $m = 4\lambda$ and $m = 5 - 4\lambda$ (Fig. 3). Such configurations seem to be occurring frequently enough to maintain a persistent activity in the lattice through cascades of nearby state changes, thereby generating activity profiles that propagate throughout the lattice. Such activity shares similar nonlinearity with Conway’s GOL, but in contrast, it is persistent without the need of any external perturbations. In this context, if Per Bak’s system operates in a ‘stimulated’ SOC regime, our system functions in a ‘spontaneous’ SOC regime.

III. SUMMARY

Scale-invariant dynamics is a striking phenomenon emerging in a large variety of spatially extended systems. Such complex systems, despite being defined by local interactions, happen to display units of equal states that organize in clusters with no characteristic size and/or duration. While scale invariance appears either in the form of self-organized criticality, or in the form of parameter-driven criticality, systems displaying such behavior are typically associated with random external inputs (e.g., random ‘grains’ of sand added in the sandpile model [10]), or with probability in interactions (e.g., temperature in the Ising model [6–8]), suggesting that stochasticity is an essential ingredient for such critical behavior. Here, we challenge this idea by investigating a purely deterministic system that displays scale-invariant dynamics in both of its forms, and show that *deterministic criticality* can also emerge in a similar fashion as in the classical model systems involving stochasticity.

Specifically, we identify critical behavior in the asymptotic dynamics of the logistic GOL, an extension of Conway’s where a single parameter (λ) tunes the rate at which sites change in every iteration [45]. Using numerical simulations of the system, we identify three distinct dynamical regimes separated by two critical deterministic phase transitions. In the first one (phase I), where $\lambda_A = 0.8750 < \lambda \leq 1$, the asymptotic dynamics of the logistic GOL is virtually the same as Conway’s GOL, with long transients that eventually settle to sparse populations of stable/oscillating structures in a spanning vacuum cluster of quiescent states [63]. The second dynamical regime (phase II) lies between $\lambda_P = 0.86055 < \lambda \leq \lambda_A$, where the logistic GOL becomes asymptotically active – i.e. the dynamics persists in the thermodynamic limit – but still with a vacuum cluster that spans the lattice. As λ decreases further, activity increases and the size of the vacuum cluster is consequently reduced. The size of this cluster decreases with λ until it disconnects into smaller clusters at λ_P . This second transition defines the limit of the third dynamical regime (phase III), $\lambda \leq \lambda_P$ where the logistic GOL is active and there is no vacuum cluster spanning the lattice.

We use standard measures from percolation theory to study the dynamics of largest clusters close to the critical point (λ_P) separating phases II and III, and find for the first time a deterministic percolation transition hidden in the Game of Life. We believe that there are two aspects that make this transition interesting. First, the study of percolation transitions – which are widespread in models of physics, networks, and population dynamics – is particularly uncommon in systems where clusters are generated by purely deterministic interactions. We are only aware of a few spatially extended [36–38] systems where transitions from homogeneous to chaotic behavior has been compared to directed percolation processes. Second, the cluster size distribution at $\lambda = \lambda_P$ has a

Fisher exponent of $\tau \simeq 1.81 < 2$, which is also not typical for percolating systems, except for a few disputed cases [19–21]. While such models suggest a new universality class, future studies on the λ_P transition would be needed to determine its universality.

Moreover, we study the system in the vicinity of transition between phases I and II, and find that λ_A marks the transition point between these phases. We find that this transition is defined by a discontinuity in the asymptotic activity, and is not related to any cluster merging process. However, we observe that the activity profiles near the border of the active asymptotic phase, i.e. when $\lambda \rightarrow \lambda_A^-$, give rise to clusters of zero-states that follow a power-law distribution (Fig. 7). We believe that this behavior reflects a peculiar form of self-organized criticality, related to the one observed in early studies of Conway’s GOL [47, 48]. Yet, the self-organized criticality observed in $\lambda \rightarrow \lambda_A^-$ is spontaneous, i.e. it does not require external inputs in order to showcase scale-invariant clusters. In this respect, it would be interesting to find other models exhibiting the same kind of behavior, and identify general underlying mechanisms to such criticality.

Overall, our study highlights the idea that scale-invariant dynamics is not limited to complex systems with stochasticity in their interactions. Specifically, we provide evidence that percolation transitions occurring in deterministic systems are similar to their counterparts observed in other classical complex systems. In addition, we also show that there are systems that exhibit self-organized criticality spontaneously in their dynamic, asymptotic attractor states, and that do not require external perturbations to display this kind of behavior.

IV. CODE AND DATA AVAILABILITY

We provide a general-purpose, open-source library for cluster analysis and criticality detection, developed to support the broader research community. This tool enables users to analyze and visualize cluster distributions and dynamics, perform power-law tests, extract key exponents such as the fractal dimension and Fisher exponent, and conduct a range of related analyses. All code and data used in this research are publicly available at <https://github.com/HakanAkgn/ClusterAnalyzer>.

A. Acknowledgments

S.J. acknowledges the computing services provided by UHEM. H.A. acknowledges funding and support from the Agency for Science, Technology and Research (A*STAR) through the SIPGA fellowship, the Scientific and Technological Research Council of Türkiye (TÜBİTAK) under TÜBİTAK 2205, and Bilkent University through the Comprehensive Scholarship. CHL acknowledges support by the Ministry of Education, Singapore (Tier-II award

number: MOE-T2EP50222-0003 and Tier-I WBS code: A-8002656-00-00).

-
- [1] G. Ódor, Universality classes in nonequilibrium lattice systems, *Reviews of Modern Physics* **76**, 663 (2004).
- [2] C. H. Lee, Generalized exact holographic mapping with wavelets, *Physical Review B* **96**, 245103 (2017).
- [3] R. Arouca, C. Lee, and C. M. Smith, Unconventional scaling at non-hermitian critical points, *Physical Review B* **102**, 245145 (2020).
- [4] S. Rafi-Ul-Islam, Z. Siu, H. Sahin, C. Lee, and M. Jalil, Critical hybridization of skin modes in coupled non-hermitian chains, *Physical Review Research* **4**, 013243 (2022).
- [5] S. Liu, H. Jiang, W.-T. Xue, Q. Li, J. Gong, X. Liu, and C. H. Lee, Non-hermitian entanglement dip from scaling-induced exceptional criticality, arXiv preprint arXiv:2408.02736 (2024).
- [6] G. Parisi and N. Sourlas, Scale invariance in disordered systems: The example of the random-field ising model, *Phys. Rev. Lett.* **89**, 257204 (2002).
- [7] R. J. Creswick and S.-Y. Kim, Critical exponents of the four-state potts model, *Journal of Physics A: Mathematical and General* **30**, 8785 (1997).
- [8] A. L. Talapov and H. W. J. Blöte, The magnetization of the 3d ising model, *Journal of Physics A: Mathematical and General* **29**, 5727 (1996).
- [9] Y. Khaluf, E. Ferrante, P. Simoens, and C. Huepe, Scale invariance in natural and artificial collective systems: a review, *Journal of The Royal Society Interface* **14**, 20170662 (2017).
- [10] P. Bak, C. Tang, and K. Wiesenfeld, Self-organized criticality: An explanation of the 1/f noise, *Physical review letters* **59**, 381 (1987).
- [11] P. Bak, Self-organized criticality, *Physical Review A* **38**, 364 (1988).
- [12] B. Drossel and F. Schwabl, Self-organized critical forest-fire model, *Physical Review Letters* **69**, 1629 (1992).
- [13] Z. Olami, H. J. S. Feder, and K. Christensen, Self-organized criticality in a continuous, nonconservative cellular automaton modeling earthquakes, *Physical Review Letters* **68**, 1244 (1992).
- [14] M. Yang and C. H. Lee, Percolation-induced pt symmetry breaking, *Physical Review Letters* **133**, 136602 (2024).
- [15] D. Stauffer, Scaling theory of percolation clusters, *Physics Reports* **54**, 1 (1979).
- [16] I. Vardi, Deterministic percolation, *Communications in Mathematical Physics* **207**, 43 (1999).
- [17] D. Stauffer and A. Aharony, *Introduction to Percolation Theory*, 2nd ed. (CRC Press, London, 1994) Chap. 2.8.
- [18] M. Sahimi, *Applications of Percolation Theory* (Taylor & Francis, London, 1994) p. 154.
- [19] M. Sheinman, A. Sharma, J. Alvarado, G. H. Koenderink, and F. C. MacKintosh, Anomalous discontinuity at the percolation critical point of active gels, *Phys. Rev. Lett.* **114**, 098104 (2015).
- [20] A. Federbush and Y. Kantor, Percolation perspective on sites not visited by a random walk in two dimensions, *Phys. Rev. E* **103**, 032137 (2021).
- [21] H. Hu, R. M. Ziff, and Y. Deng, No-enclave percolation corresponds to holes in the cluster backbone, *Phys. Rev. Lett.* **117**, 185701 (2016).
- [22] C.-K. Peng, S. Prakash, H. J. Herrmann, and H. E. Stanley, Randomness versus deterministic chaos: Effect on invasion percolation clusters, *Phys. Rev. A* **42**, 4537 (1990).
- [23] R. Beeler, R. Keaton, and R. Norwood, Deterministic bootstrap percolation on trees, *The Art of Discrete and Applied Mathematics* **5** (2021).
- [24] C. A. S. Terçariol, R. S. González, and A. S. Martinez, Analytical calculation for the percolation crossover in deterministic partially self-avoiding walks in one-dimensional random media, *Phys. Rev. E* **75**, 061117 (2007).
- [25] H. Freund and P. Grassberger, The red queen's walk, *Physica A: Statistical Mechanics and its Applications* **190**, 218 (1992).
- [26] L. A. Bunimovich, Deterministic walks in random environments, *Physica D: Nonlinear Phenomena* **187**, 20 (2004), microscopic Chaos and Transport in Many-Particle Systems.
- [27] M. C. Santos, D. Boyer, O. Miramontes, G. M. Viswanathan, E. P. Raposo, J. L. Mateos, and M. G. E. da Luz, Origin of power-law distributions in deterministic walks: The influence of landscape geometry, *Phys. Rev. E* **75**, 061114 (2007).
- [28] G. F. Lima, A. S. Martinez, and O. Kinouchi, Deterministic walks in random media, *Phys. Rev. Lett.* **87**, 010603 (2001).
- [29] D. Boyer, O. Miramontes, and H. Larralde, Lévy-like behaviour in deterministic models of intelligent agents exploring heterogeneous environments, *Journal of Physics A: Mathematical and Theoretical* **42**, 434015 (2009).
- [30] J. P. Clerc, G. Giraud, J. M. Laugier, and J. M. Luck, Electrical properties of percolation clusters: exact results on a deterministic fractal, *Journal of Physics A: Mathematical and General* **18**, 2565 (1985).
- [31] D. A. Hamburger-Lidar, Elastic scattering by deterministic and random fractals: Self-affinity of the diffraction spectrum, *Phys. Rev. E* **54**, 354 (1996).
- [32] L. Limat, Percolation and cosserat elasticity: Exact results on a deterministic fractal, *Phys. Rev. B* **37**, 672 (1988).
- [33] C. H. Lee, D. Ozaki, and H. Matsueda, Random-fractal ansatz for the configurations of two-dimensional critical systems, *Physical Review E* **94**, 062144 (2016).
- [34] A. Deger, A. Lazarides, and S. Roy, Constrained dynamics and directed percolation, *Physical Review Letters* **129**, 190601 (2022).
- [35] A. Deger, S. Roy, and A. Lazarides, Arresting classical many-body chaos by kinetic constraints, *Phys. Rev. Lett.* **129**, 160601 (2022).
- [36] H. Chate and P. Manneville, Spatio-temporal intermittency in coupled map lattices, *Physica D: Nonlinear Phenomena* **32**, 409 (1988).
- [37] P. Grassberger and T. Schreiber, Phase transitions in coupled map lattices, *Physica D: Nonlinear Phenomena* **50**, 177 (1991).
- [38] Y. Cucu, R. Livi, and A. Politi, Phase transitions in 2d linearly stable coupled map lattices, *Physica D: Nonlin-*

- ear Phenomena **103**, 369 (1997), lattice Dynamics.
- [39] M. Gardner, Mathematical games: The fantastic combinations of john conway's new solitaire game 'life', *Scientific American* **223**, 120 (1970).
- [40] P. D. Turney, Evolution of Autopoiesis and Multicellularity in the Game of Life, *Artificial Life* **27**, 26 (2021), https://direct.mit.edu/artl/article-pdf/27/1/26/2020415/artl_a_00334.pdf.
- [41] N. H. Packard and J. S. McCaskill, Open-Endedness in Genelife, *Artificial Life* **30**, 356 (2024), https://direct.mit.edu/artl/article-pdf/30/3/356/2462580/artl_a_00426.pdf.
- [42] D. A. Faux and P. Bassom, The game of life as a species model, *American Journal of Physics* **91**, 561 (2023), https://pubs.aip.org/aapt/ajp/article-pdf/91/7/561/20105275/561_1_5.0150858.pdf.
- [43] J. H. Rainwater, Self-Organization and Phase Transitions in Driven Cellular Automata, *Artificial Life* **30**, 302 (2024), https://direct.mit.edu/artl/article-pdf/30/3/302/2462558/artl_a_00437.pdf.
- [44] A. Adamatzky, *Game of life cellular automata*, Vol. 1 (Springer, 2010).
- [45] M. Ibrahimi, O. Gülsen, and S. Jahangirov, Deterministic phase transitions and self-organization in logistic cellular automata, *Phys. Rev. E* **100**, 042216 (2019).
- [46] M. Ibrahimi, A. Güclü, N. Jahangirov, M. Yaman, O. Gülsen, and S. Jahangirov, Operator representation and class transitions in elementary cellular automata, *Complex Systems* **31**, 415 (2022).
- [47] P. Bak, K. Chen, and M. Creutz, Self-organized criticality in the 'game of life', *Nature* **342**, 780 (1989).
- [48] P. Alstrøm and J. a. Leão, Self-organized criticality in the "game of life", *Phys. Rev. E* **49**, R2507 (1994).
- [49] A. P. Vieira, E. Goles, and H. J. Herrmann, Phase transitions in a conservative game of life, *Phys. Rev. E* **103**, 012132 (2021).
- [50] J. Nordfalk and P. Alstrøm, Phase transitions near the "game of life", *Phys. Rev. E* **54**, R1025 (1996).
- [51] R. A. Monetti and E. V. Albano, Critical edge between frozen extinction and chaotic life, *Phys. Rev. E* **52**, 5825 (1995).
- [52] S.-Y. Huang, X.-W. Zou, Z.-J. Tan, and Z.-Z. Jin, Network-induced nonequilibrium phase transition in the "game of life", *Phys. Rev. E* **67**, 026107 (2003).
- [53] S. M. Reia and O. Kinouchi, Conway's game of life is a near-critical metastable state in the multiverse of cellular automata, *Physical Review E* **89**, 052123 (2014).
- [54] H. J. Blok and B. Berghesen, Synchronous versus asynchronous updating in the "game of life", *Phys. Rev. E* **59**, 3876 (1999).
- [55] L. S. Schulman and P. E. Seiden, Statistical mechanics of a dynamical system based on conway's game of life, *Journal of Statistical Physics* **19**, 293 (1978).
- [56] R. M. May, Simple mathematical models with very complicated dynamics, *Nature* **261**, 459 (1976).
- [57] A. Adamatzky, *Game of life cellular automata*, Vol. 1 (Springer, 2010).
- [58] M. Newman, *Networks* (Oxford University Press, 2018) chapter 11.6.
- [59] M. E. Fisher, The theory of condensation from a lattice gas, *Physical Review A* **4**, 658 (1969).
- [60] A. Clauset, C. R. Shalizi, and M. E. Newman, Power-law distributions in empirical data, *SIAM review* **51**, 661 (2009).
- [61] J. Alstott, E. Bullmore, and D. Plenz, powerlaw: A Python Package for Analysis of Heavy-Tailed Distributions, *PLoS ONE* **9**, e85777 (2014).
- [62] A.-L. Barabási, Network science, *Philosophical Transactions of the Royal Society A: Mathematical, Physical and Engineering Sciences* **371**, 20120375 (2013).
- [63] F. Bagnoli, R. Rechtman, and S. Ruffo, Some facts of life, *Physica A: Statistical Mechanics and its Applications* **171**, 249 (1991).
- [64] R. E. Tarjan, Efficiency of a good but not linear set union algorithm, *Journal of the ACM* **22**, 215 (1975).
- [65] S. G. Krantz and H. R. Parks, *A primer of real analytic functions* (Springer Science & Business Media, 2002).
- [66] R. Shankar, *Quantum field theory and condensed matter: an introduction* (Cambridge University Press, 2017).
- [67] A. H. Land and A. G. Doig, An automatic method of solving discrete programming problems, *Econometrica* **28**, 497 (1960).
- [68] K. Christensen and N. R. Moloney, *Complexity and Criticality* (Imperial College Press, London, 2005) section 1.7.2, *Mass of a large but finite cluster at $p = p_c$* .
- [69] D. Stauffer and A. Aharony, *Introduction to Percolation Theory* (Taylor & Francis, London, 1994) pp. Section 3.4, "The Infinite Cluster at the Threshold".
- [70] Q. H. Vuong, Likelihood ratio tests for model selection and non-nested hypotheses, *Econometrica: journal of the Econometric Society* , 307 (1989).

Methods

B. Truncation of the state space and implementation of the logistic GOL

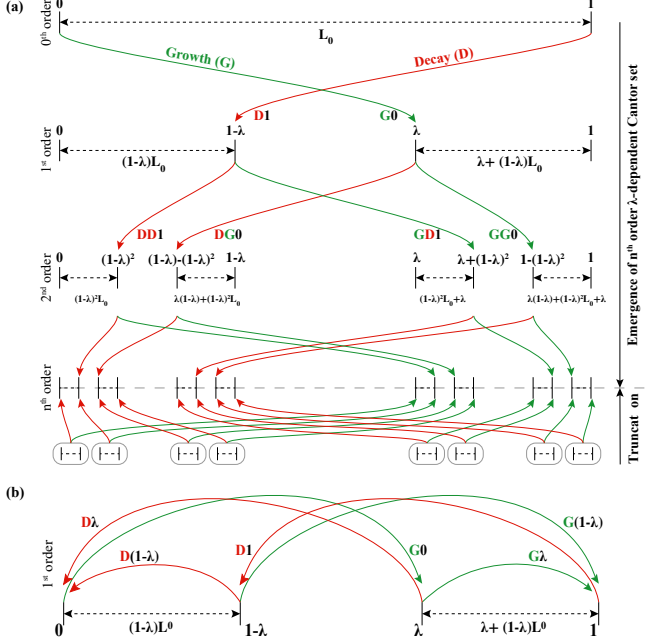


Figure 8. State space across different orders and truncation process. (a) The state space in the logistic GOL expands into a Cantor set, where the dissection ratio is set by λ . Different levels show the emergence of the first two orders of the Cantor set from applying the rules to a uniform distribution. In this study, we truncate the state space at a finite order to analyze the cluster dynamics of the system. (b) The decay and growth operations for the first order are illustrated in the truncated space. The truncation preserves the operational regimes, and lumping nearby states allows for maintaining the same dynamic behavior as the logistic GOL.

Starting from the logistic GOL, we retain only the Cantor set up to order n , truncating the rest. The state space is discretized into $L_n = 2^{n+1}$ states, which are generated recursively as follows:

$$L = \begin{cases} L_0 = \{0, 1\} \\ L_1 = \{0, 1 - \lambda, \lambda, 1\} \\ L_2 = \{0, (1 - \lambda)^2, \dots, 1 - (1 - \lambda)^2, 1\} \\ \vdots \\ L_n = (1 - \lambda)L_{n-1} \cup (L_{n-1}(1 - \lambda) + \lambda) \end{cases}$$

The set L_n represents all possible combinations of growth and decay operations on the initial set $L_0 = \{0, 1\}$. To ensure the preservation of the number of states, the map the state space onto itself:

$$s_j^{t+1} = \begin{cases} \mathbf{S}s_j^t \equiv s_j^t & \text{if } t_1 \leq m_j^t < t_2, \\ \mathbf{G}s_j^t \equiv M_{L_n}((1 - \lambda)s_j^t + \lambda) & \text{if } t_2 \leq m_j^t < t_3, \\ \mathbf{D}s_j^t \equiv M_{L_n}((1 - \lambda)s_j^t) & \text{otherwise.} \end{cases} \quad (15)$$

where M_{L_n} is defined as the nearest-element projection onto L_n :

$$M_{L_n}(x) = \arg \min_{y \in L_n} |x - y|$$

This setup with M_{L_n} ensures that each transformed state is mapped to the nearest valid state within L_n , preserving the structure and permutation of the state space. The evolution and truncation of state spaces across different orders are illustrated in Fig. 8a.

The operational domains remain the same throughout the truncation process, but now the range of Moore sum m is discretized instead of being continuous. This modification makes it possible to perform cluster analyses of the system while maintaining the features of logistic GOL with an un-truncated Cantor set. The growth/decay operations for the first-order truncation are illustrated in Fig. 8b. As the order n tends to infinity, the truncated version approaches the continuous state space of the logistic GOL. We note here that, when performing numerical simulations, the state space is nevertheless truncated in some order depending on the numerical resolution of the implementation program.

Employing the truncated version of the logistic GOL, we run $n = 10$ order simulations on a 1000×1000 grid under periodic boundary conditions (PBC). For each simulation, we discard the burn-in period of 10^5 time steps to ensure the system reaches equilibrium and then average over the next 10^5 time steps. For each λ , we run 5000 simulations and then average over the ensembles. Clusters and their sizes are obtained by connecting adjacent cells that are in the same state, realized by the *union-find* algorithm [64]. All the expected values of observables (activity, susceptibility, cluster sizes, etc.) are acquired by time-averaging and ensemble-averaging the raw data. Additionally, different initialization densities were tested and found to converge to the same thermodynamic behavior, provided the initial density supports a persistent activity.

C. Non-Analyticity of λ_A

Since the order parameter $A(\lambda)$ eventually becomes identically zero—as evidenced by numerical simulations for $\lambda > \lambda_A$ [45]—there exists $\delta > 0$ such that

$$A(\lambda) = 0 \quad \text{for all } \lambda \in (\lambda_A, \lambda_A + \delta).$$

On the other hand, we observe that

$$A(\lambda) \neq 0 \quad \text{for some } \lambda < \lambda_A.$$

According to the identity theorem for real-analytic functions[65], any function that is analytic on an interval can be represented by a convergent Taylor expansion around any point in that interval. Since $A(\lambda)$ is identically zero on the open interval $(\lambda_A, \lambda_A + \delta)$, all coefficients of its Taylor series about any point in this interval—including λ_A —must vanish. Therefore, $A(\lambda)$ must be identically zero throughout the entire connected domain where it is analytic.

In particular, this would imply:

$$A(\lambda) = 0 \quad \text{for all } \lambda \text{ in a neighborhood of } \lambda_A,$$

which contradicts the fact that $A(\lambda) \neq 0$ for $\lambda < \lambda_A$. Hence, the assumption that $A(\lambda)$ is analytic at $\lambda = \lambda_A$ must be false.

Conclusion: The function $A(\lambda)$ is non-analytic at $\lambda = \lambda_A$, and thus λ_A is a singular point of the system. Given that this transition is dictated by a single λ -neighborhood transitions, as opposed to the λ_p , its discontinuous and non-differentiable character is well justified.

For readers familiar with the Ising model, a similar argument is used to demonstrate the non-analyticity of the magnetization order parameter at the critical temperature, as revealed through the Kramers–Wannier duality[66].

D. Explicit Neighborhood of Percolation Transition λ_P

To approximate a target value, the algorithm selects a subset of Cantor set states that sum closely to the desired target within a specified tolerance. This is achieved using a branch-and-bound approach [67], which explores possible combinations of states while discarding unpromising paths. In this approach, the algorithm iteratively builds subsets of the Cantor set by adding states and checking if the current sum is within tolerance. The process is optimized by pruning paths that cannot meet the target, based on the following criteria:

- **Subset Size Constraint:** Paths that exceed the allowed number of states are discarded.
- **Tolerance Check:** Paths with cumulative sums that deviate from the target by more than the tolerance are also discarded. The tolerance is set to 0.00001 to match the resolution of our numerical simulations.
- **Feasibility Pruning:** The algorithm estimates the minimum and maximum possible sums with remaining states. Paths are pruned if they cannot reach or exceed the target based on these bounds.

This process ensures efficient exploration of feasible subsets, yielding an optimal selection that best approximates the target. Accordingly, Fig. 9 represents the

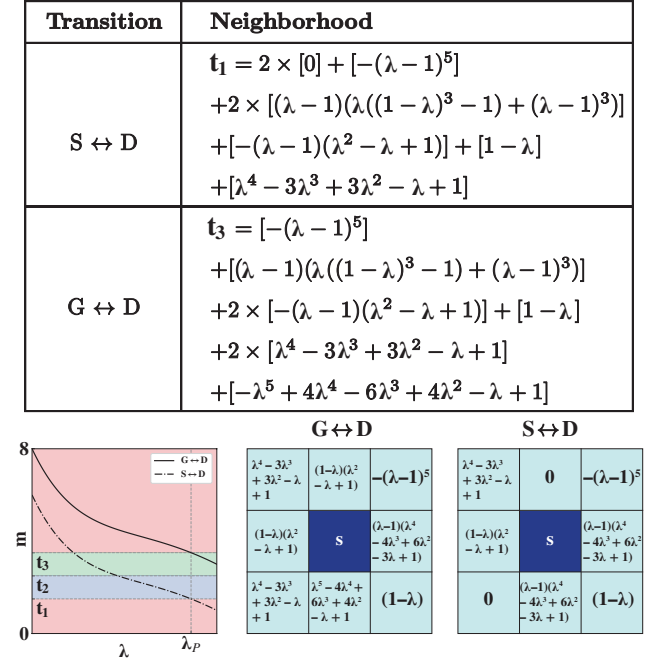


Figure 9. **Explicit operational transitions for λ_P** The table above presents the fifth-order λ neighborhood transitions for the t_1 and t_3 neighborhoods at λ_P . The panel below shows neighborhoods undergoing transition, while the lower left panel illustrates the numerical evolution of these neighborhoods as λ varies between $0 < \lambda < 1$.

5th-order Cantor set. As the percolation transition is continuous, approaching the exact percolation point λ_p with high decimal precision requires progressively higher-order neighborhoods. Fig. 3 presents the summed and simplified polynomial representations of these neighborhoods. As similar higher-order polynomials change their operational regions, neighborhood characteristics change and cluster dynamics progressively evolve. It should be noted that this selected state evolution over λ serves as an illustrative example of how changes in the operational region influence state dynamics and, eventually, cluster evolution. It does not represent an exact transition, as higher-order neighborhoods can always be found within the Cantor set.

E. Numerical Methods for Cluster Characterizations

1. Box-counting method for the capacity dimension

The box-counting method determines the capacity dimension of an object by covering it with grids of varying box sizes and counting the number of boxes, $N(\epsilon)$, that contain part of the object. By analyzing how $N(\epsilon)$ changes with the box size ϵ , the capacity dimension d_c is obtained through the following steps:

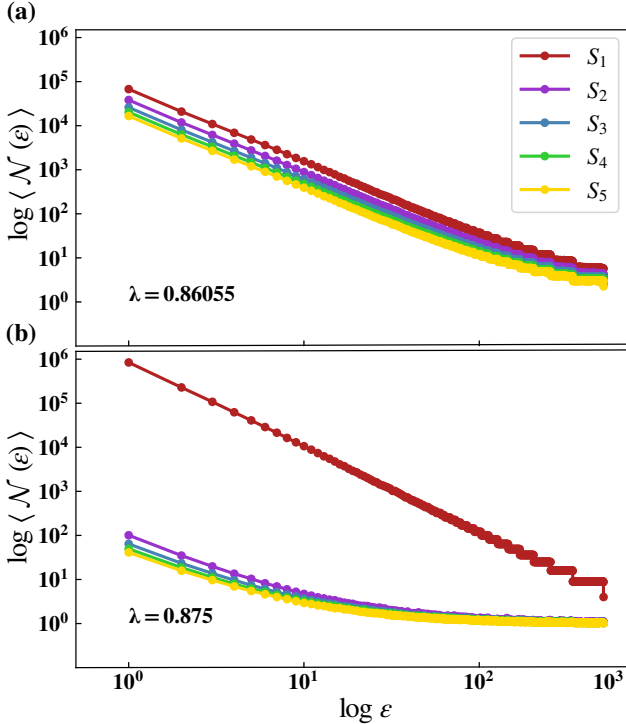


Figure 10. The capacity dimension obtained by box-counting. The plots show the (averaged) box counts $\langle N(\epsilon) \rangle$ v.s. box sizes ϵ , (a) for $\lambda = 0.86055$ and (b) for $\lambda = 0.875$. The capacity dimension equals the negative of the slope near $\epsilon = 0$. As λ increases from $\lambda = 0.86055$ to $\lambda = 0.875$, the largest cluster gradually separates from the rest, exhibiting an increasing capacity dimension, while the other clusters' capacity dimensions decrease.

1. Cover the cluster with a grid of boxes of size ϵ .
2. Count the minimal number of boxes needed to cover the cluster, denoted as $\mathcal{N}(\epsilon)$.
3. Repeat the steps above over multiple time steps and different initializations to obtain the average box count $\langle \mathcal{N}(\epsilon) \rangle$ for each box size (ϵ).
4. Plot $\log \langle \mathcal{N}(\epsilon) \rangle$ v.s. $\log \epsilon$.
5. Determine the slope of the plot in the small box size region (specifically $\epsilon = [1, 6]$). The capacity dimension d_c is given by:

$$\langle \mathcal{N}(\epsilon) \rangle \propto \epsilon^{-d_c} \quad \rightarrow d_c = -\lim_{\epsilon \rightarrow 0} \frac{\log \langle \mathcal{N}(\epsilon) \rangle}{\log \epsilon}$$

The slopes representing the capacity dimensions of the five largest clusters at two critical points are shown in Fig. 10, highlighting their distinct characteristics. Near λ_P all clusters have the same slope Fig. 10a, showing increased self-similarity of the system. Above λ_P , the largest cluster's slope increases and becomes more area-like, while other cluster slopes decrease and become more chain-like Fig. 10b. As the largest cluster percolates and

fills the entire PBC grid (excluding quiescent states), it forms a two-dimensional surface with $d_c = 2$.

However, it should be noted that the box-counting behavior holds only until the box size reaches the size of the clusters. Similar to other percolation models [68], this relationship can be understood in terms of the mass of a given cluster at the percolation threshold:

$$M(C_i, \lambda_P; \ell) = S_i(\lambda_P; \ell) \propto \begin{cases} \ell^{d_c} & \text{for } \ell \ll R_s, \\ S_i & \text{for } \ell \gg R_s, \end{cases} \quad (16)$$

where $S_i(\lambda_P; \ell)$ is the number of sites in the i -th cluster for a given window length ℓ , which corresponds to the effective box size in the counting process. When ℓ exceeds the characteristic cluster radius R_s , further increasing the window size (i.e., the effective box size) does not capture additional cluster sites; instead, the larger boxes simply encompass the existing sites, leading to no increase in the count of occupied boxes. This is because the cluster is now fully covered, meaning that regardless of additional window size increases, the same number of boxes is needed to cover the entire cluster. This results in a flattening behavior, as seen in Fig. 10b, where smaller clusters are fully covered by a constant number of boxes.

2. The scaling fits and fractal dimension at $\lambda = \lambda_P$

Fig. 11 presents the numerical fits for the scaling of cluster sizes $\langle S_i(N) \rangle$ across different percolation regimes. We perform fits on data points for system sizes N from 200 to 1000 in increments of 10. A moderate system size, such as $N = 200$, ensures statistically consistent cluster dynamics across various λ neighborhoods, independent of initial configuration. Since $\lambda = 0.86055$ does not exactly match the analytical percolation point and has additional significant decimal places beyond 0.00001, it is expected that, like other percolation models, system scaling will eventually deviate from a perfect power law [69]. Therefore, as in other percolation models, fits should be performed in the small N regime. Consequently, for our numerical fits, the small N regime [200, 1000] is selected.

Since common neighborhoods tend to decay and become passive in this regime, smaller grid sizes are sufficient for effectively capturing scaling dynamics. For these fits, we specifically use the λ values: $\lambda = 0.855$, $\lambda = 0.86055$, and $\lambda = 0.865$, respectively, for the subcritical, critical, and supercritical regimes.

In the subcritical regime (Fig. 11a), the cluster sizes follow a logarithmic scaling law $\langle S_i(N) \rangle \sim a_i \log N + b_i$, with coefficients a_i and b_i depending on the cluster rank i .

At the critical point λ_P (Fig. 11b), the scaling transitions to a power law, with the largest cluster following $\langle S_1(N) \rangle \sim N^{1.575}$, indicative of the system's fractal nature at criticality. Subleading clusters scale similarly

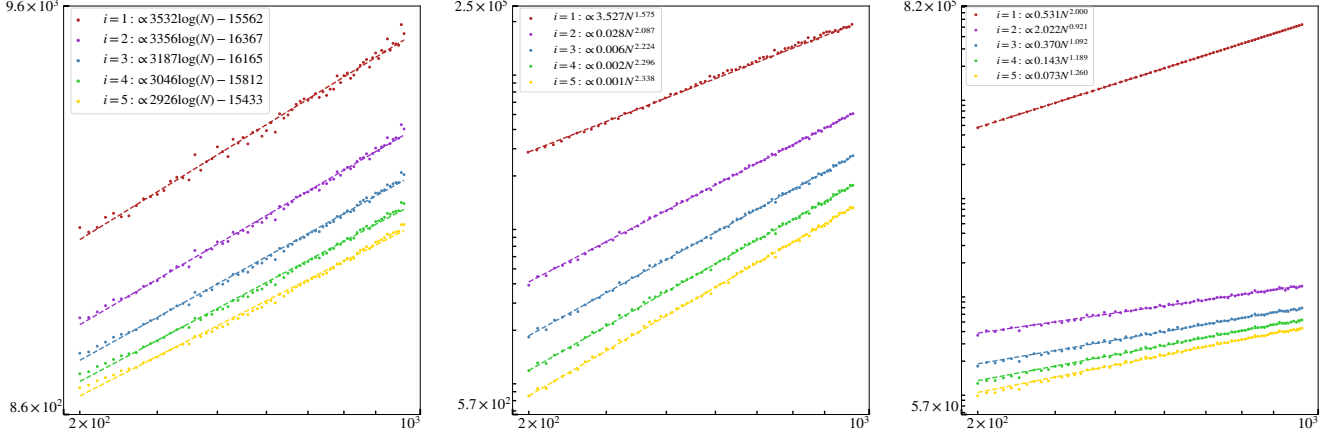


Figure 11. Numerical fits of cluster size scaling. (a) In the subcritical regime ($\lambda < \lambda_P$), cluster sizes $\langle S_i(N) \rangle$ exhibit logarithmic scaling, appearing linear in log-linear plot. (b) At the critical regime ($\lambda \approx \lambda_P$), cluster sizes scale as a power law with system size, indicating the fractal nature of the percolating cluster, appearing linear in log-log plot. (c) In the supercritical regime ($\lambda > \lambda_P$), all subleading clusters $\langle S_i \rangle$ follow logarithmic-like scaling, while the largest cluster $\langle S_1 \rangle$ scales proportionally to the system dimension, appearing linear in log-log plot.

with different exponents. These power-law fits reflect the fractal dimensions of clusters (d_f), a hallmark of critical phenomena. While the largest cluster follows a fractal scaling law, subleading clusters exhibit different exponents as a result of their sensitivity to system size and non-system-spanning nature [68]. These clusters remain fractal, scaling with exponents indicative of their distribution near criticality. Numerical fits estimate the system's fractal dimension as $d_f \approx 1.575$ with a standard deviation of $\sigma_f \approx 0.1$, reflecting deviations from the critical point λ_P in simulations. While this result is consistent with expected values near the percolation threshold, slight deviations from the exact critical point may lead to variations in the exponent.

In the supercritical regime (Fig. 11c), the largest cluster $\langle S_1 \rangle$ scales with the system's Euclidean dimension, following a numerical fit of $\langle S_1(N) \rangle \sim N^{1.9997}$, which is very close to the expected N^2 , signaling the emergence of a percolating cluster. Meanwhile, subleading clusters adhere to logarithmic-like scaling, indicating that while they grow with system size, they remain much smaller compared to the largest cluster. This analysis confirms that the scaling behavior of clusters across percolation regimes is consistent with classical percolation models.

3. The second largest cluster peak divergence

We examine how $\langle S_2(N) \rangle$ scales with system size N . The simulation was conducted over the range $\lambda \in [0.85, 0.88]$, with increments of 0.001.

It should be again noted that all top-ranking clusters, including $S_2(N)$, are quiescent clusters. As λ_P is approached, the second-largest cluster $\langle S_2(N) \rangle$ grows rapidly, as shown in Fig. 12. At λ_P , it exhibits the fastest divergence, while at nearby points, the growth is slower.

In the limit $N \rightarrow \infty$, $\langle S_2 \rangle$ shown in Fig. 4(b) diverges sharply at λ_P , signaling the emergence of a percolating cluster and the phase transition [58]. For brevity, we display only $\langle S_2 \rangle$, but the same behavior and analysis apply to other $\langle S_i \rangle$ peaks. The observed divergence of the second largest cluster peak aligns with the expectations in percolation theory.

4. Cluster size distributions from numerical simulations

We present the cluster size distributions near two critical points λ_P and λ_A in Fig. 13. We obtain the numerical

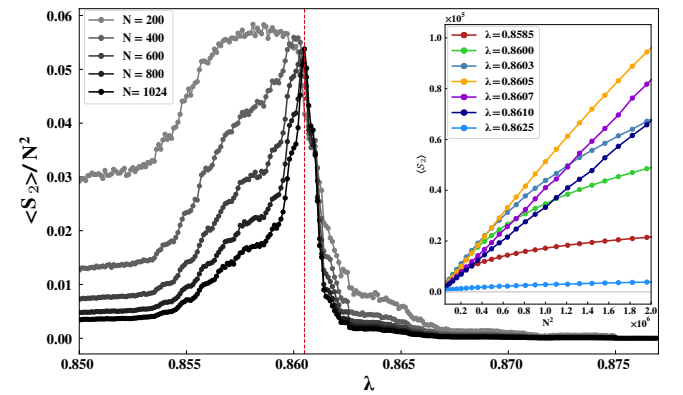


Figure 12. Size evolution of the second largest cluster with respect to the system size near λ_P . As the system approaches the critical point λ_P , the scaling rate of $\langle S_2 \rangle$ increases. As N grows larger, this results in divergence of the peak compared to nearby points. When $\langle S_2 \rangle/N^2$ is plotted this divergence manifests itself as increasing sharpness of the peak.

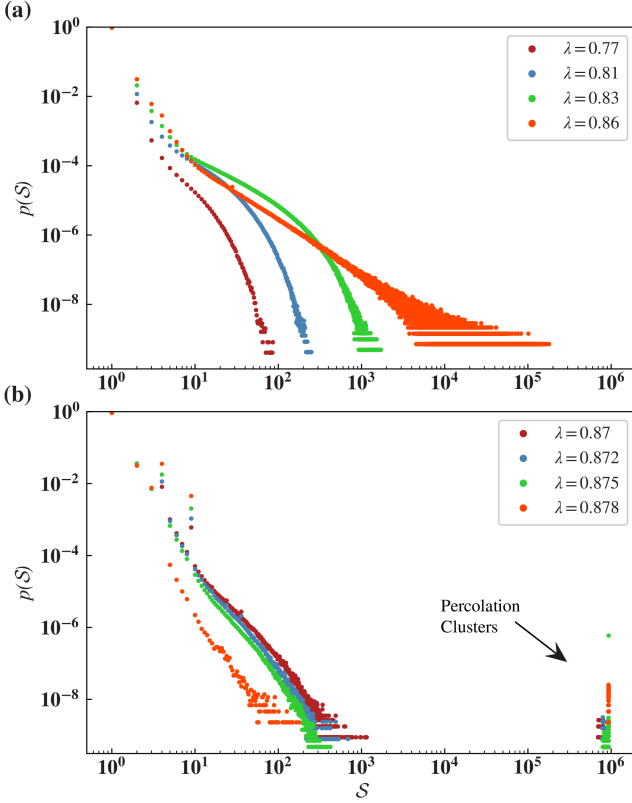


Figure 13. Log-log plot of the empirical probability density function (PDF) of cluster sizes for different λ values. (a) Evolution of PDFs towards λ_P from below shows that the PDF tails get fatter, both by shifting to higher cluster sizes and increasing the spread of the tail. At λ_P , the tail extends up to the system size, regardless of grid size, indicating scale-invariance. Constrained by the system size, the fitted power-law has an additional exponential cutoff term ($x^{-\tau} e^{-\lambda x}$). (b) Around λ_A , samples of the percolation cluster separate from the rest, piling up away at the end shown with the black arrow. At λ_A , the percolating cluster is discarded before fitting the power law, and the fitted model is a pure power law ($x^{-\tau}$). It doesn't have the cutoff term because only the percolating cluster is affected by the system size.

cal count of clusters using the *union-find* algorithm [64], and by normalizing these counts with the total number of clusters, we interpret the data as frequency distributions and treat them as probability density functions (PDFs), denoted by $p(\mathcal{S})$. At $\lambda_P = 0.86055$, the cluster size distribution $p(\mathcal{S})$ seems to follow a power law, while others around it appear as stretched exponentials (Fig. 13a). The piles at the far tail of the distributions around λ_A are contributed by the samples of percolating clusters denoted by the black arrow. After discarding the piles and truncating the lower curving head, the cluster size distribution at $\lambda_A = 0.875$ also appears to follow a power law (Fig. 13b).

Next, we define the cumulative distribution function (CDF) as the sum of probabilities up to $p(\mathcal{S} < s)$, and the

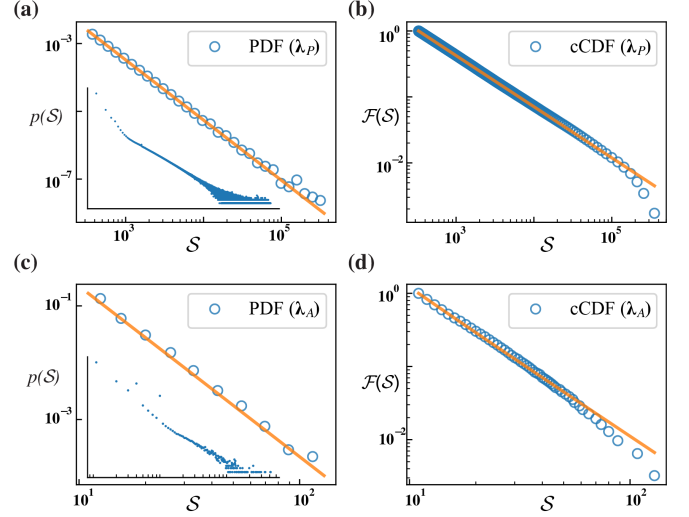


Figure 14. The results of KS method at two critical points. (a)&(c) show PDFs with *logarithmic-binning* and power-law fits by KS methods; the insets show the original PDFs (*linear-binning* and no truncation). (b)&(d) show the corresponding log-binned cCDFs with power-law fits. (a)&(b) are results at λ_P ; (c)&(d) are results at λ_A .

complementary cumulative distribution function (cCDF) as $\mathcal{F}(\mathcal{S}) = 1 - p(\mathcal{S} < s)$. To further reduce statistical fluctuations coming from each individual sample, we apply logarithmic binning, resulting in the plots shown in Fig. 5 and Fig. 6.

Previous studies have demonstrated that applying the Kolmogorov-Smirnov (KS) method to the log-binned cCDF yields more reliable results compared to applying it directly to the raw PDF [60]. This is because the cCDF and log-binning smooths out the statistical fluctuations inherent in raw data, providing a more stable statistical measure. To ensure the robustness of our results, we follow the same methodology here. Fig. 14 demonstrates *log-binned* PDF and cCDFs for λ_P and λ_A . The difference between logarithmic-binning and the conventional linear-binning is that logarithmic-binning divides the data into bins whose widths increase exponentially, which is useful for analyzing data that spans several orders of magnitude. This approach ensures that each bin contains a sufficient number of data points even in the tails of the distribution, thereby reducing noise and providing a clearer representation of the underlying distribution. In contrast, linear-binning divides the data into equally spaced bins, which can lead to sparsity and high statistical fluctuations in regions where data points are scarce, especially when dealing with heavy-tailed distributions. Note that since we set the bins' interval on log-scaled axis is the same for all plots, distributions with larger domain will have more bins – e.g., Fig. 14b has larger domain $\sim (10^2, 10^6)$ compared to Fig. 14d whose domain $\sim (10^1, 10^3)$, thus Fig. 14b has denser data points.

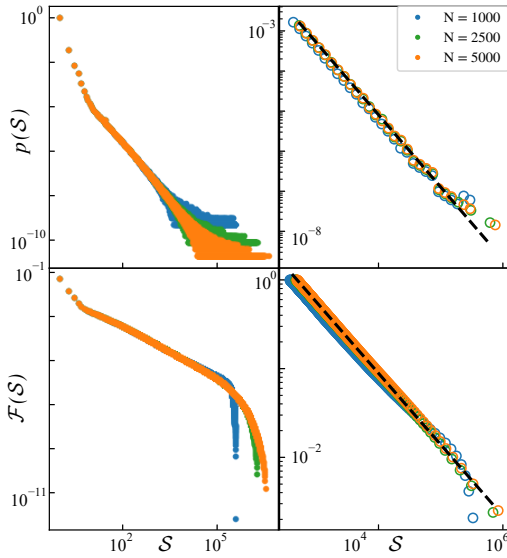


Figure 15. Grid size invariance of cluster distributions at critical threshold λ_P . **a** shows how the PDFs evolve with increasing grid size (N). As the grid size increases, the tail extends further. **b** shows the power law fits to log-binned PDFs. It can be seen that, as the grid size evolves, the PDF behavior remains consistent. **c** shows how the cCDFs evolve with increasing N . The tail extension is directly apparent, and the exponential cutoff term depends on the value of N . **d** shows the power law fits to log-binned cCDFs. It can be seen that the consistent power-law behavior is preserved across increasing grid sizes, and the fitted exponents overlap. The black dashed lines represent the power-law fits, and for all three grid sizes, the fits overlap remarkably well. We note here that for small grids where finite-size effects are apparent, KS method would decide on power-law *with exponential cutoff*; while for large grids, the power-law with exponential cutoff is no longer decisively favored over the plain power-law, and in the thermodynamic limit ($N \rightarrow \infty$), the distribution approaches a pure power-law.

5. Size Evolution of Cluster Distributions at λ_A

For λ_P , Fig. 15 shows that the cluster distribution extends up to the system size regardless of grid size (N). The exponential cutoff appears only due to the system's finite size, with the cutoff point shifting to larger values as N increases. This analysis was not performed for λ_A since criticality at λ_A is not constrained by grid size and its distribution does not extend to the system size. Consistent power-law behavior for λ_P is observed, as indicated by the overlapping on black dashed fit, confirming the presence of percolation behavior. In the power-law relation presented in Eq. 13, we use a grid size of $N = 5000$. For the plots with multiple λ points, we display samples with a grid size of $N = 1000$ due to computational limitations.

F. Kolmogorov-Smirnov Method

One important fact about empirical power-law data is that the scaling is rarely valid for the full range of the data. More often, the power law applies only for values greater than some minimum S_{\min} , i.e., only the *tail* follows a power law. Kolmogorov-Smirnov (KS) method [60–62] is proposed to determine the τ and S_{\min} , test the *goodness-of-fit*, and compare between alternative fat-tailed models via *Log-likelihood ratio test* in a principled manner.

The optimal S_{\min} minimizes the relative KS statistic between the empirical data and the fitted model while the optimal τ maximizes the likelihood of the data given the model. However, fitting the data and obtaining (τ, S_{\min}) alone does not tell us how well the power-law model fits the data; thus, we need a *goodness-of-fit* test that returns a p -value quantifying the plausibility of the power law hypothesis (p_{gf}). The closer p_{gf} is to 1, the more likely it is that the difference between the empirical data and the model can be attributed to statistical fluctuations alone. If p_{gf} is very small, the model is not a plausible fit to the data. Barabási [62, Chap. 4] suggests the model is accepted if $p_{gf} > 0.01$, while Clauset *et al.* [60] proposes a harsher threshold of $p_{gf} > 0.1$. We adopt the latter.

Even if we obtain a plausible power-law fit, it does not guarantee that the power law ($\propto x^{-\tau}$) is the best model. To rigorously assess its suitability, we must compare the power-law model against alternative fat-tailed distributions. Following the approach of Clauset *et al.* [60], we apply the KS method, including the following set of alternatives: power law with exponential cutoff ($\propto x^{-\tau} e^{-\lambda x}$), exponential ($\propto e^{-\lambda x}$), stretched exponential ($\propto x^{\beta-1} e^{-\lambda x^\beta}$), and log-normal ($\propto \frac{1}{x} \exp\left[-\frac{(\ln x - \mu)^2}{2\sigma^2}\right]$).

1. KS Statistic & KS Test

The *Kolmogorov-Smirnov statistic* (KS statistic) measures the distance of two probability distributions. It's able to quantify how *dissimilar* the empirical distribution is from the theoretical distribution / fitted model. Utilizing KS statistic, the *KS test* is a nonparametric test of the equality of probability distributions that can be used to test whether a sample came from a given reference probability distribution, i.e., to test the goodness-of-fit.

Formally, for discrete data (as the cluster sizes in our case), the KS statistic is defined as the maximum distance between the cCDF of the empirical data and the cCDF of the fitted model:

$$D = \max_{S: S > S_{\min}} |F(S) - F_{\text{model}}(S)| \quad (17)$$

Although commonly the KS statistic is defined between CDFs, it is equivalent to the above definition between cCDFs.

2. Fitting procedure

Provided that the lower bound \mathcal{S}_{\min} is known (the estimation of \mathcal{S}_{\min} is discussed later), the maximum likelihood estimator (MLE) of the power-law exponent τ is given by the solution to the transcendental equation:

$$\frac{\partial_{\hat{\tau}} \zeta(\hat{\tau}, \mathcal{S}_{\min})}{\zeta(\hat{\tau}, \mathcal{S}_{\min})} = -\frac{1}{n} \sum_{i=1}^n \ln \mathcal{S}_i \quad (18)$$

where $\{\mathcal{S}_i\}$ are all the observed cluster sizes $\geq \mathcal{S}_{\min}$. This is equivalent to maximizing the log likelihood function:

$$\mathcal{L} = -n \ln \zeta(\tau, \mathcal{S}_{\min}) - \tau \sum_{i=1}^n \ln \mathcal{S}_i \quad (19)$$

Though no closed-form solution exists for Eq. (18), one can reliably approximates τ as:

$$\hat{\tau} \simeq 1 + n \left[\sum_{i=1}^n \ln \frac{\mathcal{S}_i}{\mathcal{S}_{\min} - 1/2} \right]^{-1} \quad (20)$$

This approximation is substantially easier to compute and is accurate if \mathcal{S}_{\min} is not too small, with error decaying fast as $\mathcal{O}(\mathcal{S}_{\min}^{-2})$. If \mathcal{S}_{\min} is unknown, the estimation of \mathcal{S}_{\min} is the one minimizing the KS statistic:

$$\begin{aligned} \hat{\mathcal{S}}_{\min} &= \arg \min_{\mathcal{S}'} D(\mathcal{S}') \\ &= \arg \min_{\mathcal{S}'} \left(\max_{\mathcal{S}: \mathcal{S} > \mathcal{S}'} |F(\mathcal{S}) - F_{\text{model}}(\mathcal{S})| \right) \end{aligned} \quad (21)$$

3. Goodness-of-fit Test

To obtain the goodness-of-fit p-value, the commonly used procedure involves the following steps:

1. Take the KS distance between the empirical cCDF and the best fit, denoted as D_{real} .
2. Plug in the best-fit parameters $(\tau, \mathcal{S}_{\min})$ into Eq. (10) and generate a synthetic dataset of the same size as the original dataset. Calculate the KS distance between the synthetic cCDF and the best-fit model, denoted as D_{syn} .
3. The goal is to see if the obtained D_{syn} is comparable to D_{real} . For this, we repeat step (2.) M times ($M \gg 1$, typically $10^3 \sim 10^4$), each time generating a new synthetic dataset, eventually obtaining the $p(D_{\text{syn}})$ distribution. If D_{real} is close to the mode of $p(D_{\text{syn}})$ distribution, the power law is a considered plausible. M . is set to 2500 to obtain all our reported p_{gf} .
4. Assign a p-value (p_{gf}) to the $p(D_{\text{syn}})$ distribution:

$$p_{\text{gf}} = \int_D^\infty p(D_{\text{syn}}) dD_{\text{syn}} \quad (22)$$

The closer p_{gf} is to 1, the more likely it is that the difference between the empirical data and the model can be attributed to statistical fluctuations alone. If p_{gf} is very small, the model is not a plausible fit to the data. Barabási [62] suggest the model is accepted if $p_{\text{gf}} > 0.01$, while Clauset *et al.* [60] suggest a harsher threshold of $p_{\text{gf}} > 0.1$. We adopt the latter.

Based on this calculation, we discuss goodness of fit results for different parameter values in the range $0.8 < \lambda < 0.9$. In Fig. 16, we plot the plausibility test values, p_{gf} , to identify parameter ranges where the power law is a good fit for the cluster size distribution data from simulations. The peaks of high p_{gf} values near λ_P and λ_A (filled circles in Fig. 16) show that the power law is a plausible fit only near the critical points.

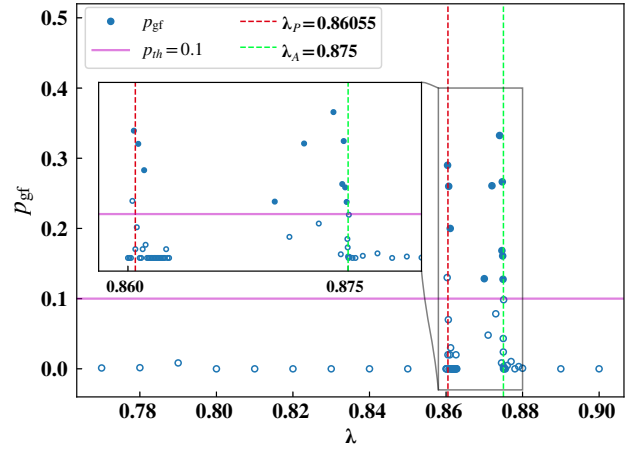


Figure 16. **Power-law fits of cluster size distributions in the logistic GOL.** The (goodness-of-fit) p_{gf} values of the plausibility test for different λ values. In points with $p_{\text{gf}} > 0.1$, the hypothesis that the distribution follows a power law is favored. Note the clear peaks exceeding 0.1 close to λ_P and λ_A in the inset. The empty circles with $p_{\text{gf}} > 0.1$ denote points where the distribution passes the plausibility test, but fails the log-likelihood ratio test.

4. Model Comparison and Statistical Results

Even if we obtain a plausible power-law fit, it does not guarantee that the power law ($\propto x^{-\tau}$) is the best model. To rigorously assess its suitability, we must compare the power-law model against alternative fat-tailed distributions. Following the approach of Clauset *et al.* [60], we apply the KS method, including the following set of alternatives: power law with exponential cutoff, exponential, stretched exponential, and log-normal. The definition of these distributions is given in Table I.

A common method to compare models is the *likelihood ratio test* – to compute the likelihood of the data

Distribution Name	$f(x)$	C
Power law	$x^{-\tau}$	$(\tau - 1)x_{\min}^{\tau-1}$
Power law with cutoff	$x^{-\tau}e^{-\lambda x}$	$\frac{\lambda^{1-\tau}}{\Gamma(1-\tau, \lambda x_{\min})}$
Exponential	$e^{-\lambda x}$	$\lambda e^{\lambda x_{\min}}$
Stretched exponential	$x^{\beta-1}e^{-\lambda x^\beta}$	$\beta\lambda e^{\lambda x_{\min}^\beta}$
Log-normal	$\frac{1}{x} \exp\left[-\frac{(\ln x - \mu)^2}{2\sigma^2}\right]$	$\sqrt{\frac{2}{\pi\sigma^2}} \left[\operatorname{erfc}\left(\frac{\ln x_{\min} - \mu}{\sqrt{2}\sigma}\right) \right]^{-1}$

Table I. Definition of the power-law distribution and other statistical distributions in our reference distribution set. For each distribution, we give the kernel $f(x)$ and the normalization factor C s.t. $\int_{x_{\min}}^{\infty} Cf(x) dx = 1$.

under two competing distributions, and take the logarithm of the ratio of the two likelihoods, denoted by \mathcal{LR} .

$$\mathcal{R} = \frac{\mathcal{L}_1}{\mathcal{L}_2} = \prod_{i=1}^n \frac{p_1(\mathcal{S}_i)}{p_2(\mathcal{S}_i)}$$

$$\mathcal{LR} = \ln \mathcal{R} = \ln \mathcal{L}_1 - \ln \mathcal{L}_2 \quad (23)$$

If \mathcal{LR} is positive, the first distribution is favored; if negative, the second distribution is favored; if close to zero, the data are insufficient to favor either model. We further apply the method proposed by Vuong [70] which gives a p -value (p_{LR}) that tells us whether the observed sign of \mathcal{LR} is statistically significant. If this p_{LR} -value is small (typically, $p_{LR} < 0.05$), then the sign is a reliable indicator of which model is a better fit to the data.

Table II presents the results of the *goodness-of-fit* and *log-likelihood ratio* tests, based on a sample size of $N = 5000$. Statistically significant p_{LR} -values are denoted in **bold**. Note that for *goodness-of-fit test results*, the larger the p_{gf} value, the more plausible the power-law model is. Whereas for *log-likelihood ratio test results*, the larger the p_{LR} -value, the less significant the sign of the test is. The final column lists our judgment of the statistical support for the power-law hypothesis at each critical point.

Alternatives to power law ($x^{-\tau}$) distribution	$\lambda_P = 0.86055$		$\lambda_A = 0.875$	
	LR	p_{LR}	LR	p_{LR}
Log-Normal $(\frac{1}{x} \exp\left[-\frac{(\ln x - \mu)^2}{2\sigma^2}\right])$	-0.189	0.69	-0.41	0.54
Stretched exponential $(x^{\beta-1}e^{-\lambda x^\beta})$	-0.97	0.61	-0.31	0.80
Exponential $(e^{-\lambda x})$	373	0.001	27.6	0.005
Power law with cutoff $(x^{-\tau}e^{-\lambda x})$	-3.89	0.005	-0.84	0.70
Verdict	Good support for power law with cutoff $p_{gf} = \mathbf{0.46}$	Good support for power law $p_{gf} = \mathbf{0.13}$		

Table II. The plausibility p_{gf} -values (*goodness-of-fit test*) for power-law and *log-likelihood ratio test* results between the power-law and alternative distributions at two critical points. Statistically significant p -values are denoted in **bold**. The plausibility values both exceeds 0.1, meaning the power-law is a plausible fit for both cases. LR is the log-likelihood ratio of power-law against alternative distributions: power-law with exponential cutoff ($\propto x^{-\tau}e^{-\lambda x}$), exponential ($\propto e^{-\lambda x}$), stretched exponential ($\propto x^{\beta-1}e^{-\lambda x^\beta}$), and log-normal ($\propto \frac{1}{x} \exp\left[-\frac{(\ln x - \mu)^2}{2\sigma^2}\right]$). If $LR > 0$, the power-law model is favored; if $LR < 0$, the alternative distribution is favored. The p_{LR} -value of log-likelihood ratio test denotes the significance of the *sign* of LR : if $p_{LR} < 0.05$, the *sign* of LR is considered significant. The ones at λ_P and λ_A indicates that power-law distribution is favored over exponential distribution. The other one at λ_P shows that power-law with exponential cutoff is favored over power-law. The final column lists the final judgments of the statistical support for the power-law hypothesis at each critical point: “with cutoff” means that the conclusion is power-law with exponential cutoff, while “good” indicates that the power-law is a good fit and none of the alternatives considered is favored. Note that this table is reported on a grid where finite-size effects is consequential; for a much larger grid, at λ_P the p_{LR} of powerlaw v.s. powerlaw with cutoff would be > 0.05 , i.e. insignificant.